UNIVERSITEIT VAN AMSTERDAM

An Exploratory Study of LHCf-triggered Events at ATLAS

by Pedro Miguel Zuidberg Dos Martires
student number: 10630120

A thesis submitted
in partial fulfilment (54 ECTS) of the
requirements for the degree of
Master of Science in Physics in the
Particle and Astro-Particle Physics track
at the University of Amsterdam

Supervisors: *David Berge, David Salek*
Examiners: *David Berge, Marcel Vreeswijk*

August, 2015

Abstract

The LHCf detector at the LHC in Geneva was conceived to put constrains on hadronic interaction models which are used in cosmic ray air shower simulations. Detecting the same interactions as ATLAS does in the central region in the very forward region, a common data taking operation was a logical choice. The complementarity of both detectors presents a unique opportunity to significantly improve hadronic interaction models.

This thesis constitutes a proof of concepts that such a common data taking is possible. Utilizing commonly recorded datasets during the 2013 proton-lead run at $\sqrt{s_{NN}} = 5.02$ TeV, we will demonstrate the successful offline matching of events from the datasets from both experiments. Moreover, a preliminary exploratory data analysis is conducted - exhibiting the benefit of the ATLAS-LHCf collaboration to the amelioration of hadronic interaction models when exploiting data collected during the 2015 proton-proton run at $\sqrt{s_{pp}} = 13$ TeV.

Contents

1 Introduction

Since the discovery of cosmic rays in 1912 by Victor Franz Hess [34], investigating their origin and chemical composition has been an ongoing venture. While the observation of the spectrum of cosmic rays in the low energy region is possible through conceptually rather simple apparatuses, such as balloon detectors [45], a more sophisticated approach has to be adopted for high and ultra high energy cosmic rays. This is simply due to the fact that the flux of directly detectable cosmic rays decreases dramatically with energy; at around 10^{15} eV it drops below one particle per square meter per year [25]. The plot in figure 1 exemplifies this circumstance. It shows the all particle flux of cosmic rays scaled by $E^{2.5}$. This makes deviations from the general power-law comportment apparent. We observe a first break in the power-law behaviour at $E \approx 3 \times 10^{15}$ eV from $dN/dE \sim E^{-2.7}$ to $dN/dE \sim E^{-3.1}$. This feature is dubbed the *Knee*. The spectrum becomes harder again in the range of $10^{18} - 10^{19}$ eV, the so-called *Ankle*. There is no general consensus on the origin of these structures in the spectrum of cosmic rays. It is however supposed, not without dispute though, that cosmic rays with energies superior to the Ankle's energy are of extra-galactic provenance [38]. A further open question is whether or not the cosmic ray spectrum extends beyond the GZK cut-off [32] at 6×10^{19} eV.

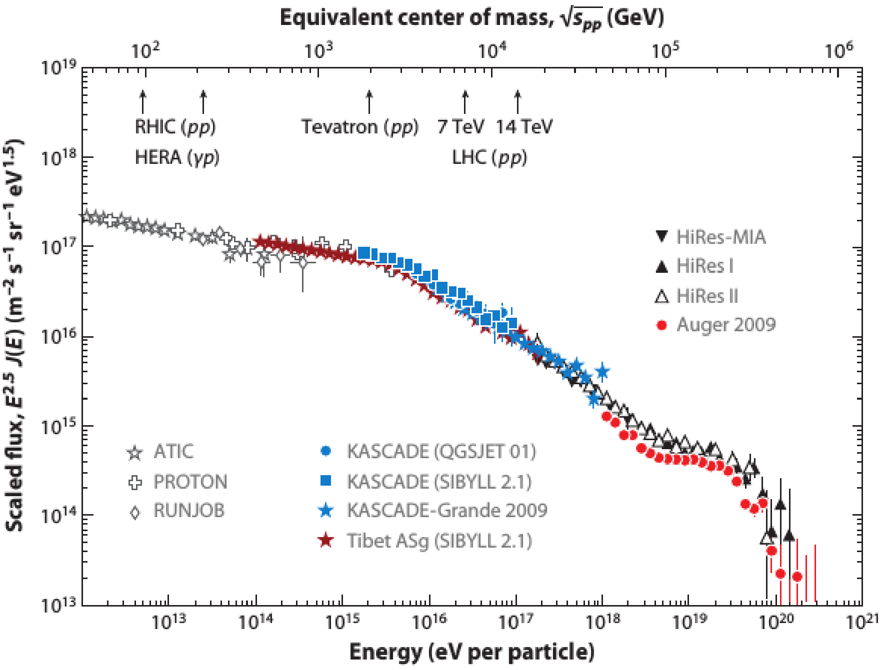

Figure 1: Energy spectrum of primary cosmic rays measured by various experiments. Note the rescaling of the energy by the power of 2.5. The energies reached by different particle accelerators are indicated in the top. [25]

Nowadays, high energy cosmic rays are detected indirectly by extensive air shower (EAS) experiments [39], such as the Pierre Auger Observatory [52], which observe secondary particles produced in the atmosphere by collisions of extraterrestrial hadrons (mostly protons but also heavier ones such as iron ions) with atmospheric molecules. The hadronic interactions that occur in these collisions are not yet very well understood, which constitutes a major problem in producing simulations of air shower physics, to which experimental data can be compared. The primary problem of air shower simulations is the calibration of the various phenomenological perturbative QCD models that simulate the hadronic interactions in the atmosphere [19]. In order to calibrate these models reliably, experimental data has to be available - an ideal source for such data is the Large Hadron Collider (LHC): the 2015 LHC proton-proton run at 13 TeV corresponds to 10^{17} eV cosmic rays in the lab frame [25]. A more thorough delineation of this issue is presented in section 2.

A particle detector conceived to improve air shower physics simulations should be able to discriminate between different phenomenological models, and at the same time be able to calibrate them to the data taken. In order to fulfil these tasks, the construction of the LHCf detector, of which a more detailed account is given in subsection 5.2, had been approved [19].

The LHCf detector is situated around Interaction Point 1 (IP1) at the LHC, sharing it with the ATLAS detector. Because both experiments observe the same particle collisions, it was an obvious choice to implement trigger sharing. This thesis presents the first ever commonly taken data by ATLAS and LHCf. One of the advantages of trigger information exchange for the LHCf experiment lies in the possibility of distinguishing between different processes that constitute the total cross section of hadronic reactions. These different processes are introduced in section 4.

Due to the lack of a simulation of the combined ATLAS-LHCf detector, a somewhat unorthodox take on the data analysis had to be adopted in this thesis, which is presented in section 3. Section 5 deals with the experimental set-up of the ATLAS and the LHCf detector. It follows, in section 6, a description of the dataset, and a perusal of the trigger sharing and event matching. In section 7 the event and track selection criteria is given. The implementation of distinguishing between the different hadronic processes (section 4) is also laid out in section 7.

The results from the common ATLAS-LHCf data analysis of the 2013 LHC lead-proton run (p+Pb) at a center of mass energy of $s_{NN} = \sqrt{5.02}$ are presented in section 8. Section 9 succeeds with showing the results from the exploratory data analysis undertaken on the ATLAS side. In the final section 10, we briefly discuss the findings of the research presented in this thesis and give an outlook on the future of the ATLAS-LHCf collaboration.

2 Motivation

We have mentioned in the introductory section that hadronic interaction models have to be improved in order to ameliorate the simulation and the understanding of extensive cosmic ray air showers. This section will elaborate further on the link between hadronic interaction models and cosmic ray air showers, and also give a motivation for and the role of the research presented in this thesis in the scope of the amendment of extensive air shower simulations.

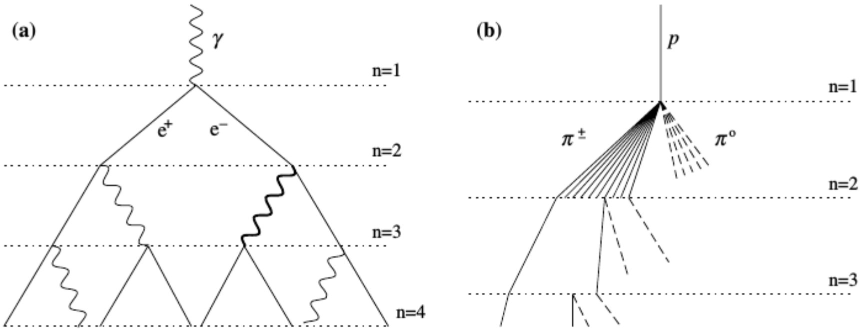

Figure 2: Schematic views of (a) an electromagnetic cascade and (b) a hadronic shower. In the hadron shower, dashed lines indicate neutral pions which do not re-interact, but quickly decay, yielding electromagnetic subshowers (not shown). Not all pion lines are shown after the n = 2 level. [43]

In figure 2 are schematically depicted the two kinds of air showers, electromagnetic and hadronic ones. EAS experiments on the ground detect the product particles of such electromagnetic or hadronic particle cascades. In order to determine the mass composition of cosmic rays by analysing the product particles at the earth's surface, the chain reactions in the earth's atmosphere have to be simulated. A chain of 8-10 hadronic reactions, for example, leads to detectable muons on the ground in the 20-200 GeV range [22].

While electromagnetic and weak interactions are well understood by means of perturbative quantum field theory within the Standard Model [33], the understanding of strong interactions is still limited and is the main source of uncertainty in the simulation of cosmic ray air showers [56]. This means that amending hadronic interaction models is crucial to a confident interpretation of the abundance of excellent data from cosmic ray air shower experiments.

By analysing data from general purpose detectors such as ATLAS, important constraints have already been put on parameters of hadronic interaction models [23]. To further constrain interaction model parameters, also particle collision products in the forward region, which is not covered by ATLAS but by LHCf, have to be studied. Due to large uncertainties in the extrapolation of hadronic interaction models to higher energies, strong constraints are needed to reliably extrapolate findings at accelerator energies to cosmic ray physics. Figure 3 exemplifies the uncertainties present in such extrapolations on the instance of the production cross section of proton-air interactions.

$$\sigma_{prod}^{p-air} = \sigma_{tot}^{p-air} - \sigma_{el}^{p-air} - \sigma_{qel}^{p-air} \tag{1}$$

where "el" stands elastic and "qel" for quasi-elastic [24]. Reliable extrapolations are needed for the simulation of a set of reference showers without which determining the type of the primary particles and estimating the mass composition of cosmic rays is not possible [8].

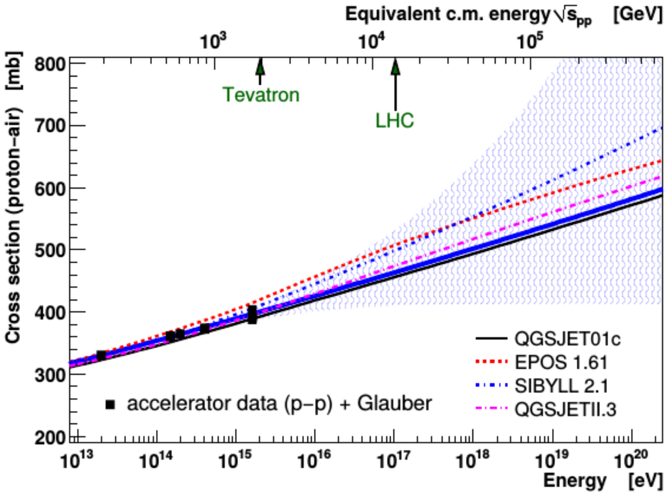

Figure 3: Uncertainty of the extrapolation of the proton-air cross section, σ_{prod}^{p-air}, from accelerator to cosmic ray energies. (The accelerator data stems from pre-LHC times.) [55]

The research presented in this thesis is first and foremost a proof of concept that a combined analysis of ATLAS and LHCf, which will help to refine hadronic interaction models, is indeed realizable. A primary step was to verify the correct functioning of the trigger sharing and event matching between both experiments which is explained in section 6.2. Moreover, rudimentary information on kinematic variables were exchanged, demonstrating the feasibility of a future comprehensive combined ATLAS-LHCf analysis. While the proof of concept presented here was undertaken on a proton-lead dataset from 2013 with $\sqrt{s_{NN}} = 5.02$ TeV, the combined ATLAS-LHCf analysis that will eventually be used to further constrain hadronic interaction models will investigate proton-proton collisions at $\sqrt{s_{pp}} = 13$ TeV from the 2015 LHC run.

The reason why to favour commonly taken data from the proton-proton collisions over the proton-lead collisions is because usually the proton-proton scattering total cross section is taken as an input to fix basic parameters in all hadronic interaction models [50]. Moreover, the center of mass energy is higher, allowing for the refinement of constraints at higher energies.

3 Exploratory Data Analysis (EDA)

In modern-day (astro-)particle physics various distinct statistical approaches are being deployed for analysing datasets [41]. Amongst the most prominent approaches one finds the frequentist, the Bayesian or also the χ^2 approach. Despite their sharp differences of philosophy, these different approaches might yield the same outcome of a statistical analysis of a certain dataset; which results in scientists not being aware of the aforementioned differences throughout their scientific career.

As in particle physics a different approach often leads to different results for the analysis of a dataset, scientists in this field are rather scrupulous when applying one approach or the other and interpreting the result when drawing conclusions. This awareness of the philosophical differences entrains fierce disputes on the validity of the different approaches. In spite of their differences, all particle physicists compare their experimental signal to prediction, analytical or Monte Carlo generated. Moreover, these different approaches are all of a quantitative nature and by using any of these approaches one can test the validity of one's prediction, i.e. hypothesis.

Nowadays, when it comes to analysing experimental data, the work of an experimental particle physicist consists almost exclusively of testing a certain hypothesis. However, predictions are not always available, either no simulation has been performed or there is no theoretical model available that makes sound forecasts. In this case, one cannot rely on the quantitative approaches mentioned above. This does not mean there is nothing to be learned from data in such an instance.

A well-established approach, yet not well known in the physics community, towards data that is not backed by theoretical predictions is Exploratory Data Analysis (EDA). EDA has been developed by the statistician John W. Tukey who also produced the first comprehensive account on this matter - *Exploratory Data Analysis* [53]. EDA is a complementary approach to statistical hypothesis testing i.e. confirmatory data analysis (CDA). EDA and CDA tackle the problem of drawing conclusions from data from diametrically opposed antecedents. While CDA tries to confirm a certain theoretical hypothesis, EDA explores data in order to postulate hypotheses that potentially lead to new experiments and data collections.

What classifies EDA is, according to Tukey, not so much using particular tools rather than having a certain mindset [54]. The attitude, when analysing data in the scope of EDA, is one of trying to find patterns in data that are not apparent in the first place. The goal is not so much to give answers but to be able to ask the right questions. Techniques generally applied in EDA are inter alia box plots, histograms, multi-vari charts and Tukey's trimean [53]. The latter one being a quantitative tool and the others being graphical instances of techniques used in EDA.

Although there is no exact definition of EDA in the tradition of Tukey, one can characterize it by the following features [11]:

- grasp the meaning of data
- focus on graphically representing data

- tentatively build models, refine and respecify them
- be flexible in the choice of applied methods (e.g. histograms, multi-vari charts)

Although Exploratory Data Analysis is not very common in particle physics, it has proven itself to be very useful in other academic areas such as social sciences [29] or in the analysis of social networks [49].

3.1 EDA in this thesis

When starting the research presented in this thesis, no simulation of proton-lead collisions encompassing the ATLAS and the LHCf detector at the same time had been available. In order to make any meaningful statements about the commonly taken data of ATLAS and LHCf, an approach different to the orthodox hypothesis testing had to be found.

In a first step, we opted for comparing histograms and scatter plots of minimum bias events and events that fired off the LHCf-trigger. Comparing these events allows for making first assumptions about the key differences between minimum bias physics and forward physics.

Subsequently, after having identified the track multiplicity as the most intriguing kinematic variable, we focussed on retrieving first rudimentary physics statements from analysing it further by *"playing around"* with data (which is in the mindset of EDA).

We will show in section 9 that this approach enables us to identify eminent qualities of very forward physics, when compared to transversal physics, which are paramount to the development of a future combined simulation of the ATLAS and LHCf detectors, and ultimately to the simulations of cosmic ray air shower physics.

4 Inelastic Collisions

In order to gain a better understanding of cosmic ray air shower physics, it is important to clearly determine a particle collision's nature. We can divide them into three categories: elastic, diffractive and non-diffractive collisions. In an elastic collision no quantum numbers are exchanged between two nuclei; only a transfer of momentum occurs. These collisions are relatively easy to distinguish from the others as the outgoing and incoming particles are identical. This is not true for differentiating between non-diffractive and diffractive events. In what follows we are going to give a theoretical account of diffractive collisions and identify the presence of so-called *rapidity gaps* as a signature of such collisions. Rapidity gaps flag regions of the detector in which no particles have been produced.

Diffractive collisions can furthermore be subdivided into single diffractive (SD), double diffractive (DD) and central diffractive (CD)[1]. This yields then for the total cross section:

$$\sigma_{tot} = \sigma_{elastic} + \sigma_{SD} + \sigma_{DD} + \sigma_{CD} + \sigma_{non-diff.} \tag{2}$$

---

[1] SD, CD an d CD are note the only possible diffractive processes. An additional process is the so-called *single plus double diffractive* (SDD) process. Information on it can be found in this paper [6]

In particle collisions involving heavy nuclei a further class of events called *ultra-peripheral collisions* (UPC) can be found. They constitute a non-negligible part of the total non-diffractive cross section. In section 4.2 we are going to give a brief explanation of UPC events which also elucidates why isolating them from other non-diffractive events makes sense.

4.1 Diffractive collisions

In high energy particle collisions at the LHC, products of inelastic collisions are generally evenly spread in the central region. For instance, the average spread between 2 product particles of a proton-proton collision is of 0.15 units of rapidity [3]. With a particle's rapidity defined as:

$$y = \frac{1}{2}\ln\frac{E+p_L}{E-p_L} \tag{3}$$

where E denotes the particles energy and p_L its longitudinal momentum. However, rather large rapidity spreads between two product particles are produced when in the t-channel a color singlet exchange takes place. At high energies, electroweak channels, which include for example exchanges of π^0s, are suppressed, compared to strong force channels [10]. It is these strong processes where no net exchange of color takes place that are dubbed *diffractive*. The colorless state through which the process takes place is called the *pomeron*. It arises theoretically in the scope of the Regge formalism of QCD [10, 15]. Diffractive processes constitute at LHC energies approximately $25-30\%$ of the total inelastic cross section; with central diffractive collisions being suppressed by a factor of 10 in comparison to SD collisions. A schematic depiction of the three different kinds of diffractive processes is given in figure 4. In the SD case the pomeron excites one of the two nuclei which then dissociates, leaving the other nucleus intact. In DD collisions both nuclei get excited and dissociate and in CD processes each nucleus radiates off a pomeron which then produces particles in the central region.

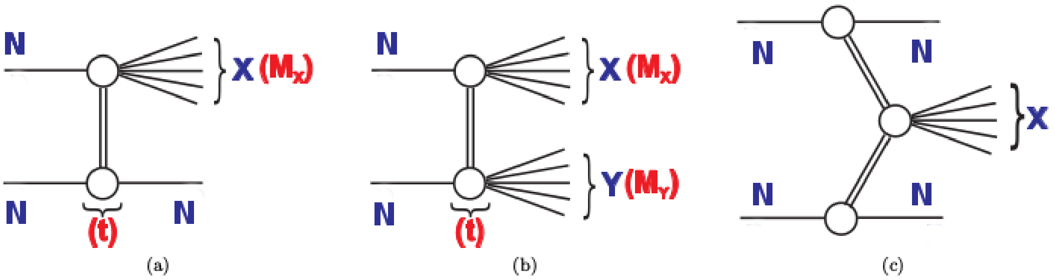

Figure 4: Schematic illustrations of the single-diffractive dissociation (a), double-diffractive dissociation (b) and central diffractive (c) processes and the kinematic variables used to describe them. By convention, the mass M_Y is always smaller than M_X in the double dissociation case and $M_Y = M_N$ in the single dissociation case, M_N being the intact nucleon's mass. [3]

A useful approximation of the rapidity (cf. equation 3) in high energy physics is the pseudorapidity η:

$$\eta = \frac{1}{2}\ln\frac{|\vec{p}| + p_L}{|\vec{p}| - p_L} \text{ , for } |\vec{p}| \gg m \tag{4}$$

with $\vec{p}$ being the particles momentum and m its mass.

When using $E = \sqrt{p_L^2 + p_T^2 + m^2} \approx p_L + \frac{p_T^2}{2p_L} + \frac{m^2}{2p_L}$ $(p_L \gg m, p_T)$, we can approximate the rapidity also differently:

$$\begin{aligned} y &= \frac{1}{2}\ln\frac{E + p_L}{E - p_L} \\ &= \frac{1}{2}\ln\frac{(E + p_L)^2}{E^2 - p_L^2} \\ &= \frac{1}{2}\ln\frac{E^2 + p_L^2 + 2Ep_L}{p_L^2 + p_T^2 + m^2 - p_L^2} \\ &= \frac{1}{2}\ln\frac{p_L^2 + p_T^2 + m^2 + p_L^2 + 2Ep_L}{p_T^2 + m^2} \\ &\approx \frac{1}{2}\ln\frac{2p_L^2 + 2Ep_L}{p_T^2 + m^2} \\ &\approx \frac{1}{2}\ln\frac{2p_L^2 + 2p_L^2}{p_T^2 + m^2} \\ &\approx \ln\frac{2p_L}{\sqrt{p_T^2 + m^2}} \end{aligned} \tag{5}$$

Before we proceed, we need also an approximation for a particle's momentum at high energies using the squared centre of mass energy s. When dealing with two incoming particles with four-momenta p_x^μ and p_y^μ, respectively, and two outgoing systems with four-momenta p_X^μ and p_Y^μ, respectively, then [10]:

$$\begin{aligned} \vec{p}_i^{\,2} &= \frac{1}{4s}\lambda(s, m_x^2, m_y^2) \\ \vec{p}_j^{\,2} &= \frac{1}{4s}\lambda(s, M_X^2, M_Y^2) \end{aligned} \tag{6}$$

where $i = x, y$ and $j = X, Y$, and with $\lambda(x, y, z) = x^2 + y^2 + z^2 + 2xy + 2xz + 2yz$. Requesting $s \gg m_{i,j}$ we obtain:

$$|\vec{p}_{i,j}| \approx \frac{\sqrt{s}}{2} \tag{7}$$

We can now tackle the issue of calculating the rapidity spread, i.e. the rapidity gap, between the two remnant systems of a two-body scattering. We call the invariant masses of the remnant systems M_X and M_Y (cf. figure 4) with the convention $M_X > M_Y$.

Going back to the approximation derived in equation 5 we see that the rapidity takes its maximal value for $p_T \to 0$. Plugging in also the relation in equation 7 ($|\vec{p}| \to p_L$) we get for the maximal rapidity of the Y-system:

$$|y_Y|_{max} = \ln \frac{\sqrt{s}}{M_Y} \tag{8}$$

The maximal rapidity is obtained when the corresponding incoming nucleus does not dissolve at all, or when its remnants are in the narrow forward η region. The latter happens when the invariant mass of the nucleus' remnants are of the same order of magnitude as the invariant mass of the nucleus itself, this means that the transverse momenta of the remnant particles tend to zero. A small gain of transverse momentum is exactly the signature of a diffractive event [3] - under the condition of not being elastic.

For the X-system, if we assume a dissolution of the corresponding ingoing nucleus over a wide range of rapidity, we have to suppose a distributions of different rapidity values for the different remnant particles. To find the lower bound of the rapidity, we assume that we have a particle with a transverse momentum in the order of magnitude of the invariant mass of the system: $p_{T,y_{min}} \approx M_X$. In order to find the longitudinal momentum of the particle with the smallest rapidity, we assume that the ingoing momentum $|\vec{p}_{in}| \approx \frac{\sqrt{s}}{2}$ (cf. equation 7, which has only a longitudinal component) is distributed evenly over the rapidity region in which tracks are present [10]. This results in a longitudinal momentum component for the particle with minimal rapidity of:

$$p_{L,y_{min}} = \frac{m_x}{M_X} \frac{\sqrt{s}}{2} \tag{9}$$

Plugging everything now into equation 5 and remembering that $m_x \approx M_Y$ we get:

$$|y_X|_{min} \approx \ln \frac{M_Y \sqrt{s}}{M_X^2} \tag{10}$$

By taking the difference of equation 8 and equation 10 we obtain the rapidity gap between systems X and Y.

$$\begin{aligned} \Delta y &\approx (y_Y)_{max} - (y_X)_{min} \\ &\approx \ln \frac{\sqrt{s}}{M_Y} - \left(-\ln \frac{M_Y \sqrt{s}}{M_X^2} \right) \\ &\approx \ln \frac{s}{M_X^2} \end{aligned} \tag{11}$$

The extra minus sign arises because the sign of y is different for both systems. Just like we have approximated the rapidity y by the pseudorapidity η in equation 4 we can now also approximate the rapidity gap with the pseudorapidity gap.

$$\Delta \eta \approx \ln \frac{s}{M_X^2} \tag{12}$$

At LHC energies the pseudorapidity distribution of non-diffractive (ND) events is presumed to be flat. This means that the particle density $\rho_N = dN/d\eta$ vs. η is constant [30]. By Poisson statistics, the probability to have no particles in a certain region, i.e. to have a rapidity gap of size $\Delta\eta$, is given by $P_{gap}^{ND}(\Delta\eta) = e^{\rho_N \Delta\eta}$ [31]. This shows us that pseudorapidity gaps are exponentially suppressed in non-diffractive events at LHC energies. With this last statement we have shown that rapidity gaps are a unique signature of single diffractive and low M_Y double diffractive events.

Although we haven't shown it here, rapidity gaps are also signatures for other diffractive processes - for instance general DD collisions. Showing this would go beyond the scope of this thesis. The reader can consult for example references [6, 10, 31] for further insight. In figure 5 are depicted the rapidity gap signatures for SD, DD and CD collisions.

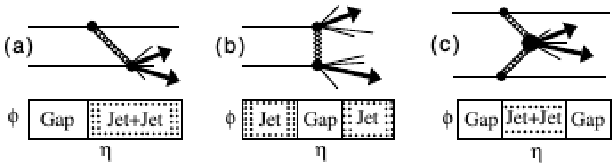

Figure 5: Schematic illustrations of the single-diffractive dissociation (a), double-diffractive dissociation (b) and central diffractive (c) processes with the corresponding $\Delta\eta$ signatures [30]

4.2 Ultra-Peripheral collisions

In an ultra-peripheral collision (UPC) the proton does not interact with the lead nucleus itself but with the Lorentz contracted electromagnetic field that encases the nucleus. This electromagnetic field can be considered as consisting of (quasi)-on-shell photons which excite the proton into a higher mass state, such as Δ^+, with only a small transfer of transversal momentum taking place between the lead and the proton nuclei [13]. The excited mass state subsequently decays into a charged and a neutral particle, yielding for instance the following reaction chain:

$$p + \gamma \to \Delta^+ \to n + \pi^+ \tag{13}$$

Here the charged particle is a pion and the neutral particle a neutron. The neutron can be detected in the very forward region by the LHCf detector. However, because the LHCf collaboration seeks to improve hadronic interaction models, it makes sense to implement cuts that reject UPC events. This is explained in section 7.3. UPC events are expected to show no activity in the central region. Figure 6 schematically illustrates a ultra-peripheral collision.

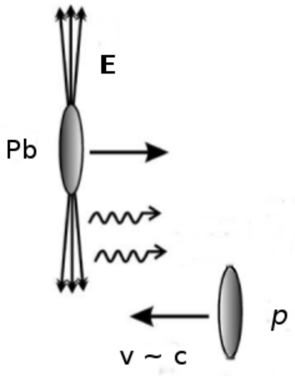

Figure 6: In p+Pb collisions the proton can interact with Lorentz contracted electric (and magnetic) fields surrounding the lead nucleus. The interaction between the proton and these fields can be replaced by an interaction between the proton and real (or quasi-real) photons. [12]

5 Experimental Set-Up

The 26.7 km long LHC ring is divided into 8 sectors (sectors 12, 23, 34, 45, 56, 67, 78 and sector 81, cf. figure 7). Interaction Point 1 (IP1) is situated where sector 12 and sector 81 meet [28]. A schematic overview of the alignment of the detectors in the LHC accelerator ring is shown in figure 7. Two of the detectors placed around IP1 are the ATLAS experiment and the LHCf experiment ("f" for forward). While ATLAS is designed to study high transversal momenta physics, LHCf focusses on forward physics. In the following two subsections we provide a more profound description of both detectors, with emphasis on the parts of the detectors that are mentioned in section 7.

5.1 The ATLAS detector

As we are going to make extensive use of the pseudorapidity in section 7 lets firstly clearly state the convention used at ATLAS and LHCf. The positive pseudorapidity region at ATLAS and LHCf is defined as the region lying in sector 81 (figure 7). This side is also referred to as *side A*. The negative η region lies in sector 12, also called *side C*. ATLAS uses a right handed coordinate system with the z-axis being aligned along the beam pipe. The pseudorapidity η is defined as $\eta = -\ln\, tan(\theta/2)$. Where θ is the polar angle of the spherical coordinates (r, θ, ϕ). In the transversal plane ATLAS uses cylindrical coordinates (r, ϕ, z). Where r is the radial component and ϕ the azimuthal angle.

When implementing the track selection cuts and the reconstruction of pseudorapidity gaps, information from the Inner Detector and the calorimeters of ATLAS is required. What follows is a brief explanation of the parts of the Inner Detector and the calorimeters referred to in section 7, succeeded by a description of the Minimum Bias Trigger Scintillator (MBTS), as it will provide the trigger signal employed on the ATLAS side.

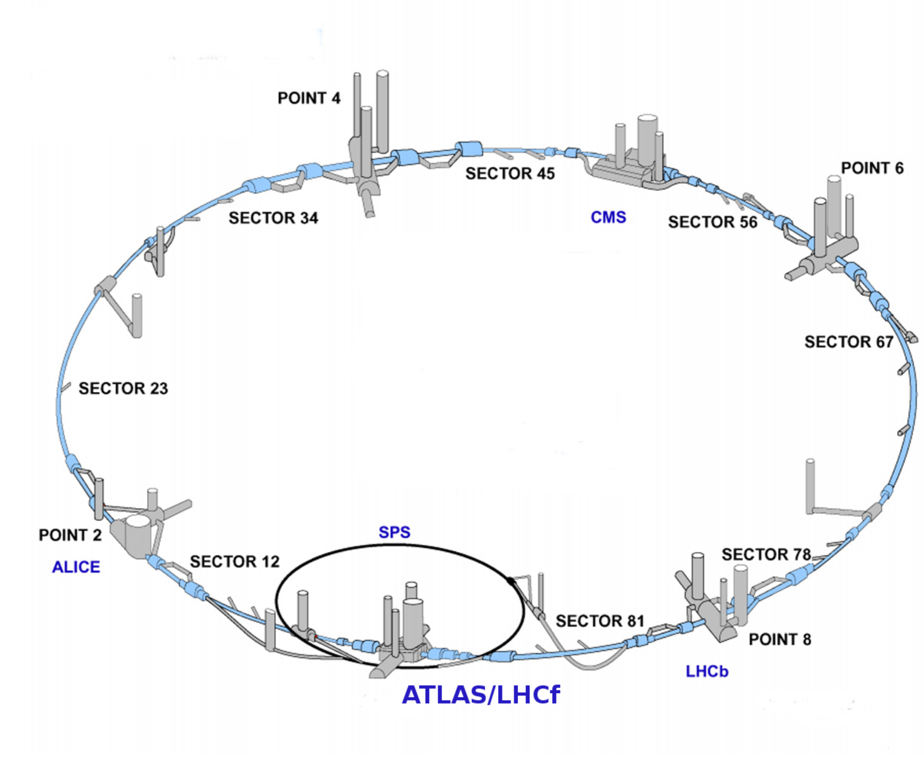

Figure 7: Schematic view of the LHC ring - showing the position of the four big experiments (ALICE, ATLAS, CMS, LHCb). [2]

5.1.1 The Inner Detector

The inner detector of ATLAS, consisting of the Pixel Detector, the Semiconductor Tracker (SCT), and the Transition Radiation Tracker, is immersed in a 2 T solenoid magnetic field. The positioning of the sub-detectors of the Inner Detector is shown in figure 5.1. The Inner Detector allows for track reconstruction in the pseudorapidity region of $|\eta| < 2.5$. The Pixel Detector and the SCT are needed when implementing track selection cuts, described in section 7. We are now giving more information on these two sub-detectors.

Pixel Detector: The Pixel Detector is the innermost sub-detector of the Inner Detector. It is constituted of 3 barrel layers and 6 disk layers of which the layer closest to the beam pipe, dubbed B-layer, is the most important one in track and vertex reconstruction. A minimum of three space points in the Pixel Detector enables tracking and vertexing at ATLAS [35].

Semiconductor Tracker: The SCT is composed of individual active silicon strip detector modules; 2112 in the barrel and 988 in each endcap. The barrel lies in the central region and is made up of four cylindrical layers. Nine additional annular layers on side A and side C of the barrel form the endcaps [47].

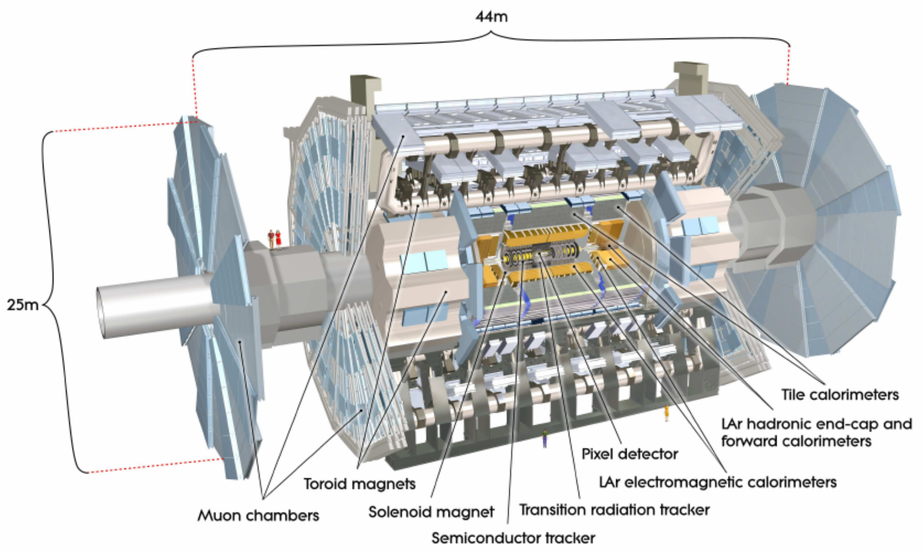

Figure 8: Cut-away view of the ATLAS detector [16].

5.1.2 Calorimeters at ATLAS

When determining the pseudorapidity gaps, for the classification of inelastic events, one needs, in addition to reconstructed tracks, also the reconstructed clusters in the calorimeters. In the central rapidity region of ATLAS, electromagnetic and hadronic calorimeters, jointly covering the $|\eta| < 4.9$ [16] region, have been implemented. In figure 9 their respective positions are shown. Focussing on the pseudorapidity coverage, a short description of the single parts is given below. More detailed information can be found in reference [16].

LAr electromagnetic calorimeter: The LAr electromagnetic calorimeter consists of three apart components, the barrel component and the two endcaps. Each of these has its own cryostat. The barrel, covering $|\eta| < 1.475$, consists itself of two identical half barrels and the endcaps are comprised of two coaxial wheels, an outer and an inner one - covering the regions $1.375 < |\eta| < 2.5$ and $2.5 < \eta < 3.2$, respectively [16].

Tile calorimeter: Surrounding the LAr EM calorimeter, the barrel and the extended barrel of the Tile calorimeter cover pseudorapidity regions $|\eta| < 1$ and $0.8 < |\eta| < 1.7$, respectively. The Tile calorimeter is a steal/scintillator tile sampling calorimeter reaching from 2.28 m to 4.25 m away from the beam pipe [16].

LAr hadronic endcap calorimeter: Similar to the LAr EM endcap calorimeter, the LAr hadronic endcap (HEC) calorimeter consists of two independent wheels. These wheels constitute a sample calorimeter with copper as the absorber and LAr as the active medium. The same cryostat is used in both forward calorimeters. The LAr HEC calorimeter's pseudorapidity regions covered are $1.5 < |\eta| < 3.2$; slightly overlapping with the range of the LAr forward calorimeter and the Tile calorimeter [16].

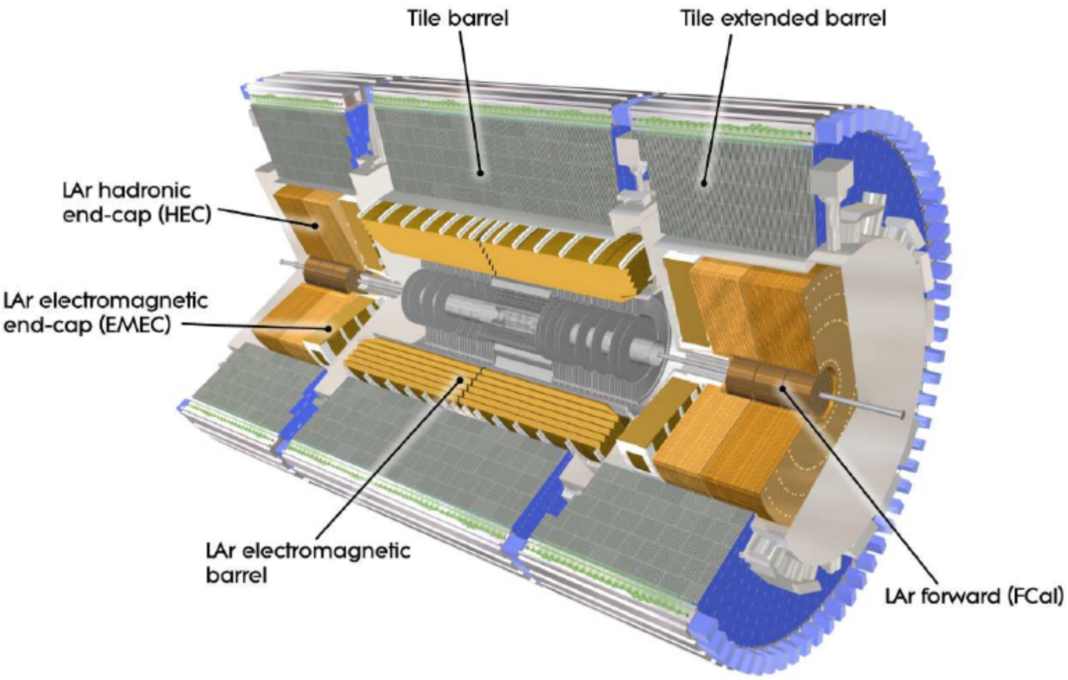

Figure 9: Cut-away view of the ATLAS calorimeter system. [16]

LAr forward calorimeter: The Forward Calorimeter (FCal), which is integrated into the endcap cryostats, consists of three modules in each endcap. A copper one, followed by two tungsten modules. The former is optimized for electromagnetic showers, whereas the later two mainly detect hadronic interactions. Each module is constituted of tubes and rods. In the spacing between these, the liquid argon forms the sensitive medium of the calorimeter [16].

5.1.3 Minimum Bias Trigger Scintillator

Located on side A and C between the Inner Detector and the LAr calorimeters, the Minimum Bias Trigger Scintillator (MBTS) covers a pseudorapidity range of $2.1 < \eta < 3.8$. On each side, the MBTS consists of a panel of 16 scintillator plates arranged into an outer and an inner ring. Noise events are suppressed by setting the trigger threshold to 40 mV for a hit in any of the plates [40].

Minimum bias events are generally associated with non-diffractive events, which produce hits in the MBTS on both sides with an expected amplitude around 100mV. As the definition of a minimum bias event is detector dependent, one cannot expect only non-diffractive events being triggered. We have to assume non-negligible contributions to MBTS events from diffractive channels, especially single and double diffractive ones [40].

5.2 The LHCf detector

140m away from IP1, on side A and C, is placed a neutral particle absorber (TAN) to protect the D2 dipoles (figure 10) from neutral particles emerging in collisions at IP1. Charged particles are swept away by the D1 dipoles. The LHCf detector modules are installed inside the TANs, where the module placed on side A is denoted Arm1 and the one on side C Arm2 [19]. This particular position of the LHCf detector arms, just upstream of the BRAN luminosity monitors [21] and the ATLAS ZDCs [36], allows for a pseudorapdity coverage of the very forward region, i.e $|\eta| > 8.4$.

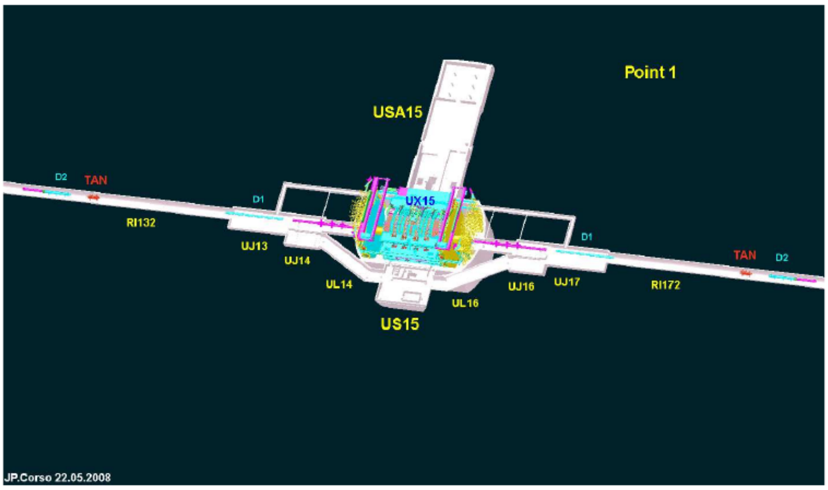

Figure 10: LHCf set-up around Interaction Point 1 (IP1). The structure shown in the center represents the ATLAS detector which surrounds IP1. The two arms of the LHCf detector are situated 140m away from IP1 on each side of the beam pipe. Their location is indicated in the schema by 'TAN' (Target Neutral Absorber). [19]

The main purpose of LHCf, as already stated earlier, is to discriminate between different hadronic interaction model such as SIBYLL 2.1 [7], QGSJET-II [46] or DPMJET-III [51] and to calibrate them. Moreover, LHCf might spark new interaction models [19]. The information provided by ATLAS to LHCf allows for a classification of processes in a data driven way, which brings additional precision to constraints to be imposed onto models of cosmic ray air shower physics and motivates once more the trigger sharing operation. We will elucidate this point further in section 7.3.

5.2.1 Arm2 detector

In the 2013 p+Pb run only the Arm2 detector, located downstream of the proton remnant side, was taking data. For this reason we will only characterize the Arm2 module here. (Although both detector arms work on the same principle, there are differences.) Figure 11 shows a picture of the Arm2 module.

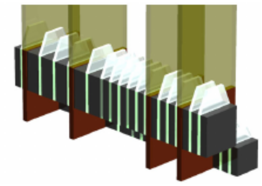

Figure 11: Schematic depiction of the LHCf Arm2 detector. Transverse sizes: $25 \times 25\text{mm}^2$ for the Tower Small (TS) and $32 \times 32\text{mm}^2$ for the Tower Large (TL). [20]

Arm2 is a sampling and imaging calorimeter with plastic scintallator plates as the active material, interleaved with tungsten plates. Moreover position sensitive silicon strips are inserted. [28] As can be seen in figure 11, Arm2 consists of two towers. Their pseudorapidity coverage is $-\infty < \eta < -9.6$ for the Small Tower (TS) and $-9.5 < \eta < -8.5$ for the Large Tower (TL). The longitudinal dimension for both towers corresponds to 44 radiation lengths and 1.55 hadronic interaction lengths. The calorimeter attends an energy resolution of $< 5\%$ for electromagnetic showers and $\approx 40\%$ for hadronic showers.

An event at LHCf is recorded when a trigger signal is issued. This happens when three ore more successive scintillator plates record a trigger threshold level of 150 MeV. That threshold level corresponds in about to a 100 GeV threshold for incident gamma-rays. [19, 37] The trigger efficiencies lie at 100% for an incidient photon with an energy above 100 GeV and 70% for an incident neutron with an energy superior to 500 GeV [26, 27].

6 Sharing trigger information

As mentioned already earlier, no simulations of the detector response are available for the whole ATLAS-LHCf detector ensemble and it is not possible to directly compare data obtained from particle collisions to MC-simulations. The analysis strategy pursued in section 9 is a comparison between events that were triggered by LHCf, by using the *EF_L1LHCF_NoAlg* trigger, to events triggered by the ATLAS trigger *EF_L1MBTS_1_1_NoAlg*. The LHCf-trigger fires on activity in the LHCf Arm2 as described in the previous section. The ATLAS trigger requires at least one hit on side A and side C in any of the 16 scintillator plates of the MBTS wheels; selecting minimum bias events (cf. section 5.1.3).

Antecedent to any data analysis at ATLAS using the LHCf trigger signal, the correctness of the trigger sharing between ATLAS and LHCf had to be demonstrated. In order to do so, the events that were independently enregistered at ATLAS and LHCf had to be matched to each other. Prior to the research presented here, this had never been done. The confirmation of successful trigger sharing is outlined in this PubNote [13]. For the sake of completeness and because the successful trigger sharing was a major part of the research conducted in the scope of this Master's project, we are going to restate the trigger sharing and event matching procedure.

6.1 The dataset

The 2013 LHC p+Pb run is subdivided in three periods: a pilot period and periods A and B. The data analysed in this thesis stems from period A. In this period, the proton flew into the negative η region, i.e. from side C to side A and vice versa for the lead ion. The proton was accelerated to 4 TeV and the lead nucleus to $4 \times \frac{Z}{A} \approx 4 \times \frac{82}{208} = 1.58$ TeV [48]. The low luminosity conditions during the p+Pb lead to a 3% pileup[2] probability [1]. In the dataset produced on the ATLAS side, which will be analysed in this thesis, about 3.3 million events were recorded.

6.2 Trigger sharing and event matching

The decision whether or not to register an event is implemented at ATLAS and LHCf by using trigger chains. These consist of three levels: Level1 triggers, Level2 triggers and Event Filter triggers. The former is a hardware trigger and the latter two are software trigger algorithms. Only events passing a trigger chain running in active mode are recorded. The ATLAS trigger system is conceived to record events at a rate of about 200 Hz. However, $p + Pb$ collisions exceeded this rate at peak luminosities and a prescale factor had to be applied in order to randomly select events not to be registered. This reduces the number of events passing the trigger chain and keeps the recording rate below 200 Hz.

If an event passes the three levels of a trigger chain running in active mode, then the event is registered. For registered events, one can always check which Level1 trigger bits are set. This mean that if for example an event passed the *EF_L1LHCF_NoAlg* trigger we can access the Level1 trigger bit information of the *EF_L1MBTS_1_1_NoAlg* trigger. This tells whether or not the event fired the *L1MBTS_1_1* trigger, regardless of it not passing the *EF_MBTS_1_1* trigger chain. This might be due prescaling at any of the trigger levels or simply not passing the trigger requirements.

The trigger *EF_L1LHCF_NoAlg* sent from LHCf to ATLAS uses no additional information at the Event Filter level, the trigger is thus solely relying on information from LHCf. The same counts for the *EF_L1MBTS_1_1_NoAlg* trigger signal, it relies only on information from ATLAS and is completely independent of LHCf. During the common data taking operation of ATLAS and LHCf an event is registered if a event passes a ATLAS trigger chain or if a trigger signal is issued to ATLAS from LHCf - indicating that an event passed a LHCf trigger chain. These first three paragraphs of this section are mainly based on references [5, 18].

Due to prescaling and the independence of the LHCf-trigger, not all events that fired off the trigger at LHCf were recorded at ATLAS. Therefore, a one to one event matching was not possible and the following procedure had to be applied. The ATLAS Central Trigger Processor calculates a UTC time stamp derived from a GPS-based time stamping system with a stability of 5 ns and high absolute time precision of 20 ns [9]. The

---

[2] Secondary particle collisions between two incident nuclei occurring in addition to the primary particle collisions are referred to as pileup. [42]

accumulated count of the LHC 40 MHz bunch crossing signal provides a time stamp for LHCf with a resolution better than 25ns [28]. This time stamp does not provide absolute time since it is reset at the beginning of each LHCf run. However, it will be useful for the event matching since it precisely determines the relative time intervals between the acquired events. It constitutes a high precision relative time stamp and with a time difference between two consecutive bunch crossings of 2 μs it does clearly separate the events lying in a single LHCf run. To differentiate between the different LHCf runs, which are generally a couple of minutes long, a lower precision absolute time stamp was consulted. This time stamp is provided by the readout PC with a precision of 10 μs.

For each LHCf run, identified by the absolute time stamp provided by the readout PC, a number of randomly chosen reference events in the LHCf dataset was then matched to events in the ATLAS dataset by utilizing absolute time stamps and the relative time difference between the events recorded on either side. The remaining events in the datasets were matched by their relative time difference to the randomly chosen reference events. ATLAS and LHCf were able to link through this procedure 99.7% of the recorded events at ATLAS, for which a LHCf-trigger signal arrived, to an event at LHCf. The remaining 0.3% of ATLAS events had no counterpart at LHCf because at the end of each LHCf run a few events were missed to be recorded.

We confirmed the successful offline event matching by using so-called *Bunch Crossing Identifiers*. A bunch crossing is defined as a 25 ns time-window centred on the instant at which a nuclei bunch may cross Interaction Point 1. Per LHC turn, a maximum of 3564 bunch crossings occurs. [4] ATLAS and LHCf attribute separately to each bunch crossing a Bunch Crossing Identifier (BCID) from 0 to 3563. By comparing the BCIDs, we corroborated the successful offline event matching using relative time stamps. In figure 12 the succeeded event matching is illustrated and figure 13 displays two of the matched events.

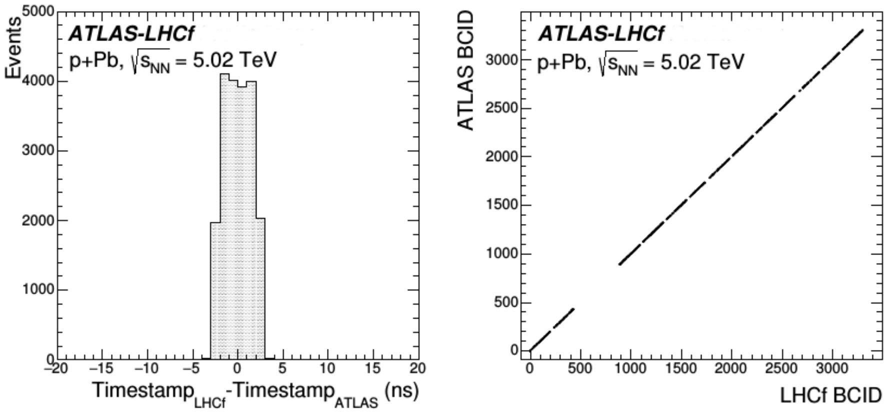

Figure 12: Left: The difference of the time stamp of the events recorded by ATLAS and LHCf. Right: The exact agreement of the BCIDs of the events matched based on the time stamp. [13]

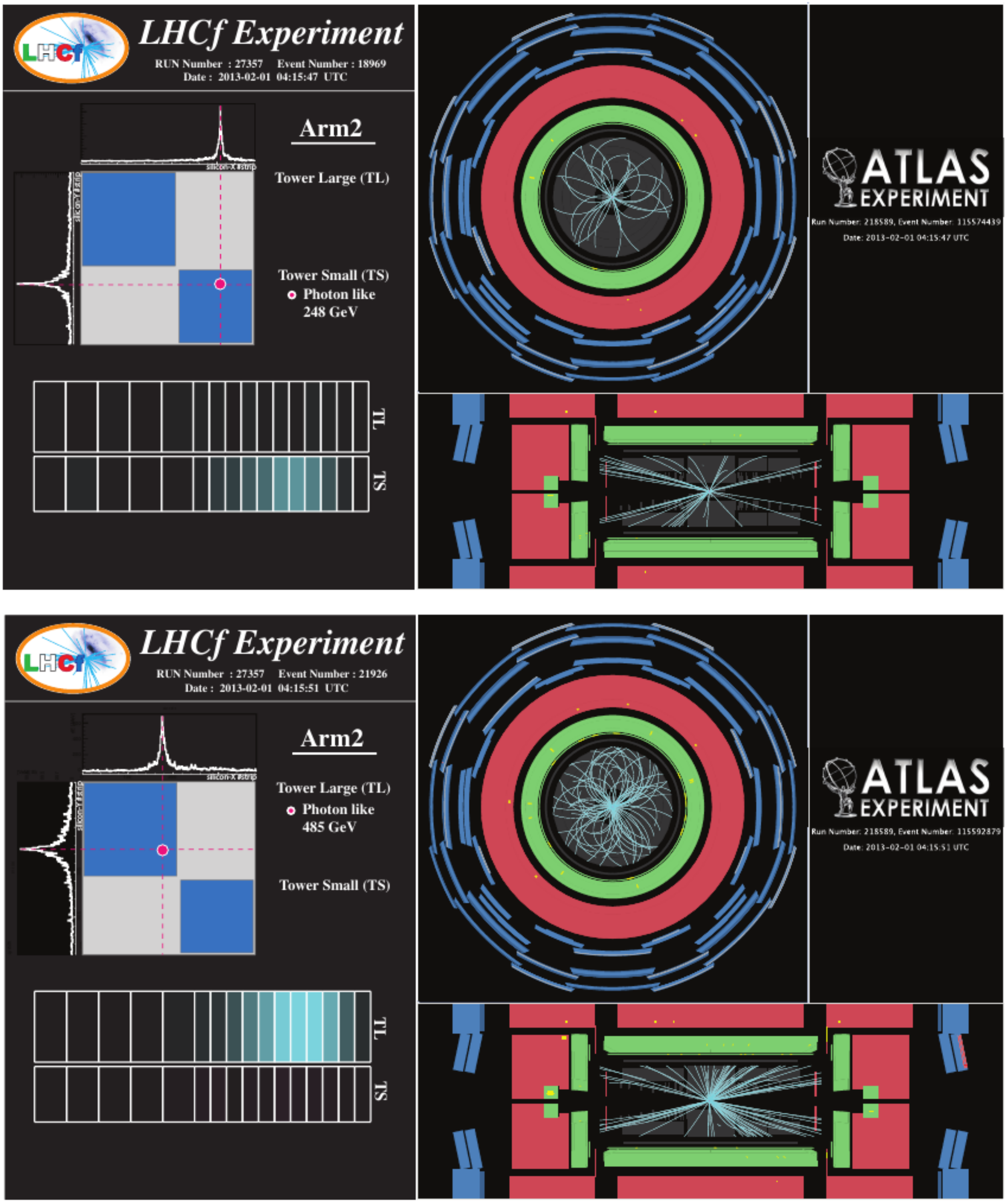

Figure 13: Event displays of two matched events, with a photon like particle reconstructed in TS (top) and TL (bottom) in the LHCf Arm2 module. The LHCf display shows hit position measured by the silicon strip sensors (top) and the deposited energy in the sampling calorimeters (bottom). The ATLAS display shows the reconstructed tracks of charged particles (blue lines) in the inner detector and the energy deposited in the calorimeters (yellow squares) [13].

7 Data Analysis

In section 7.3 we show how the separation between non-diffractive, diffractive and UPC events is done. In order to do so, we need information on reconstructed tracks. Section 7.1 describes which track selection cuts were applied on these. The reconstruction of rapidity gaps, which is needed to differentiate between diffractive and non-diffractive events, is laid out in section 7.2.

7.1 Track selection

The track selection cuts applied in the analysis presented in this thesis are based on the standard charged particle track selection used for proton-proton collisions [17]. In addition, cuts specific to heavy ion collisions were applied [48]:

- track author requirement that corresponds to inside-out tracking algorithms only:
  - *trk_PatternReco1* & 1 or *trk_patternReco2* & 16
- phase space cuts on transverse momentum p_T and pseudorapidity η:
  - $p_T > 100$MeV
  - $|\eta| < 2.5$
- track requirements in the Semi Conductor Tracker (SCT):
  - $\geq$ 2, 4, 6 SCT hits for $p_T \in$ 100-200, 200-300, and $>$ 300 MeV respectively
- track requirements in the Pixel detector:
  - $\geq$ 1 Pixel hit(s)
  - at least one hit in the B-layer if one is expected
- track requirements on the transverse impact parameter d_0 and longitudinal impact parameter $z_0 \sin\theta$:
  - $|d_0|$, $|z_0 \sin\theta| < 1.5$mm (d_0 and z_0) constructed with respect to primary vertex
  - $|\sigma_{d_0}/d_0|$, $|\sigma_{z_0 \sin\theta}/(z_0 \sin\theta)| < 3$

We did not apply any specific event selection cuts usually deployed in minimum bias studies, such as requiring at least one reconstructed vertex, because those would not have been generally compatible with LHCf-triggered events: it will be shown that a high fraction of events does not contain any particles within the tracker acceptance, preventing a primary vertex to be reconstructed.

In order to ensure the quality of the data, we did however check whether or not an event was listed in the *Good Run List*. The Good Run List encompasses events for which the detector operated in conditions suited for physics analysis. For each event included in the *Good Run List*, we determine the number of tracks that pass the aforementioned cuts and denote them n_{sel}.

7.2 Reconstruction of pseudorapidity gaps

In subsection 4.1 we saw that large rapidity gaps are a signature of diffractive events. We are now going to lay out the reconstruction of rapidity gaps. In section 5.1.2, we have seen that the ATLAS calorimeters cover the rather large pseudorapidity region of $|\eta| < 4.9$. This makes them well suited to utilize them in the reconstruction of pseudorapidity gaps. In order to determine the presence of rapidity gaps, the energy deposited in each cell of the different calorimeters is studied separately. In the $|\eta| < 2.5$ region, calorimeter information is supplemented by reconstructed tracks that passed the cuts described in section 7.1 - increasing thus the sensitivity in the very central region.

The reconstruction of pseudorapidity gaps can only be done in the context of a set threshold. In our analysis we took $p_T^{threshold} = 0.2$ GeV, leaving us with an additional cut on reconstructed tracks of $p_T > p_T^{threshold}$ and with the same cut on the transverse momentum of clusters in the calorimeters [48].

To find rapidity gaps, we subdivided the $|\eta| < 4.9$ region into 98 rings covering $\delta\eta = 0.2$ each. The rapidity gaps on side A and side C of an event were then determined by counting the number of consecutive rings that are free of clusters/tracks, starting the counting at the edges of the detector at $\eta = \pm 4.9$. Dividing the number of consecutive activity free rings by 10 on the $-\eta$ side yields the proton rapidity gap $\Delta\eta_p$. Doing the same on the $+\eta$ side gives us $\Delta\eta_{Pb}$.

When lying out the reconstruction of rapidity gaps, we left out one minor complication: each of the cells in the calorimeters has a noise. The cell noise is in general well described by a Gaussian with standard deviation σ_{noise} [3]. By comparing the deposited energy E in a cell to the root mean square of the electronic noise in that cell, we are able to limit the influence of the noise on the rapidity gap reconstruction. This is implemented by tightening the standard cut on the cell significance $S = E/\sigma_{noise}$ (standard cut: $S \geq 4.0$). Where σ_{noise} stems from data from empty bunch crossings. Here are the applied cuts on the cell significance for the different subcalorimeters [48]:

- $S \geq 5.0$ for clusters originating in the EM Barrel
- $S \geq 4.8$ for clusters originating in the EM End Cap
- $S \geq 4.6$ for clusters originating in the Hadronic End Cap
- $S \geq 5.4$ for clusters originating in the Tile Calorimeter
- $S \geq 4.4$ for clusters originating in the FCal

In figure 14 we see the effect of imposing the above mentioned cell significance thresholds S_{th}. The probability P_{noise} for producing a noisy cell in a ring goes down to $P_{noise} \lesssim 10^{-3}$. In order to calcultate P_{noise} we first need the probability $P(S_{th})$ for noise fluctuations producing a significance S that passes S_{th} [3]:

$$P(S_{th}) = \frac{1}{\sqrt{2}} \int_{S_{th}}^{\infty} e^{-S^2/2} dS \tag{14}$$

P_{noise} can now be calculated by:

$$P_{noise} \simeq N \times P(S_{th}) \tag{15}$$

where N is the number of cells per ring. N variates between 10 in the outer part of FCal to about 4000 in the central region [3].

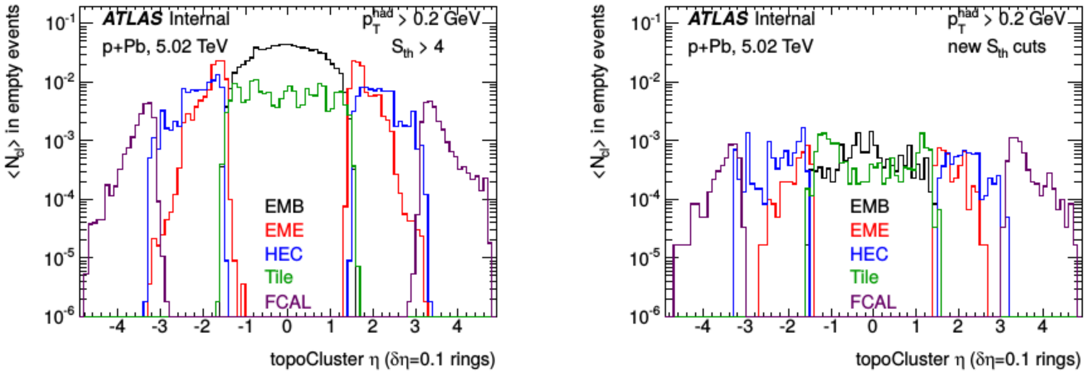

Figure 14: Mean number of clusters N_{cl} with $p_T > 0.2$ GeV in empty events for all clusters (left) and after significance cuts (right), in 2013 data. The histograms have been normalized to the total number of events, effectively giving te probability P_{noise}. [48]

The method of rapidity gap reconstruction, presented in this section, will allow us to discriminate between diffractive and non-diffractive minimum bias events [3]. In addition, we are going to demonstrate the validity of utilizing the rapidity gap method on events that fired off the *EF_L1LHCFS_NoAlg* trigger.

7.3 Distinguishing diffractive, non-diffractive and UPC events

We have seen in section 4 the different kinds of inelastic collisions occurring at the LHC. With the content of sections 7.1 7.2, we are now able to experimentally discriminate between these. In section 5.1.3 we stated that MBTS-triggered events are generally associated with non-diffractive events. However, a non-negligible share of events is expected to origin from diffractive events [40]. In order to eliminate diffractive events from the data collection of MBTS-triggered events, we apply a cut on the rapidity gaps:

- requiring $\Delta\eta_{Pb} < 2.0$ and $\Delta\eta_p > 2.0$, removes events with diffractive excitations of the lead nucleus (single diffractive)
- requiring $\Delta\eta_{Pb} > 2.0$ and $\Delta\eta_p < 2.0$, removes events with diffractive excitations of the proton (single diffractive)
- requiring $\Delta\eta_{Pb} < 2.0$ and $\Delta\eta_p < 2.0$, removes events with diffractive excitations of the lead nucleus and the proton (double diffractive)

In section 4.2 we saw that UPC events produce neutral and charged particles in the very forward region. The charged particle gets swiped out by the dipole D1 and only the neutral particle travels on along the beam pipe. The neutral particle then induces a trigger signal in the LHCf detector. By requesting the absence of tracks in the ATLAS Inner Detector, UPC events can be suppressed.

The remaining problem is to disentangle diffractive and non-diffractive events in LHCf-triggered events, as the rapidity gap method described in this section was developed for minimum bias events. We saw however in section 4.1 that for non-diffractive events rapidity gaps are exponentially suppressed. This means that any event, which is not UPC or elastic and which exhibits rapidity gaps, is of a diffractive nature. We are going to corroborate this statement in section 9 in a data driven way.

8 First common ATLAS-LHCf analysis

In this section, whose content is based on reference [13], we are going to show results from the first common ATLAS-LHCf data analysis. This means that information on particle collisions gathered at ATLAS and LHCf separately was utilized to concoct the here presented plots.

Figure 15 shows the energy spectra for hadron-like and photon-like events in the Small Tower and the Large Tower of the LHCf detector Arm2. Using the number of reconstructed tracks at ATLAS, on which no track selection was applied, the events are categorized in zero multiplicity events ($n_{sel} = 0$) and events with $n_{sel} > 0$. We observe a clear difference of the energy spectrum between both selections for hadron-like events in the Small Tower (bottom left), which covers the $\eta < -9.6$ pseudorapidity region. We see furthermore that the zero multiplicity events dominate and cause the peak in the energy spectrum. The long tail up to 10 GeV is due to the 40% energy resolution for hadronic events.

Simulations show that neutrons produced in UPC events, cf. equation 13, have a mean energy of 3.5 TeV and exceed so the LHCf trigger threshold, cf. section 5.2.1. We can conclude that the characteristic peak in the hadron-like energy spectrum around 3.5 TeV in TS is caused by exactly these UPC events, as there is no peak apparent in all the other energy spectra displayed in figure 15.

Figure 16 displays the scattering angle of particles enregistered by LHCf, calculated using the reconstructed impact location in LHCf. The data points below and above 140 μrad correspond to TS and TL, respectively. We observe again a strong effect of the $n_{sel} > 0$ selecion in the Small Tower (scattering angle < 140 μrad).

Moreover, figure 16 shows a Monte Carlo simulation[3] of UPC and QCD processes. It predicts that the UPC contribution can be significantly suppressed by rejecting events

---

[3] UPC events are simulated using the Weizsäcker-Williams method [57] for calculating the flux of quasi-on-shell photons around the lead ion and using the SOPHIA model [44] for the event generation of photon-proton collisions. For QCD events DPMJET3.04 [14] is deployed. Resolution effects and efficiency losses have been incorporated neither for LHCf nor for ATLAS.

with no reconstructed tracks in ATLAS, as no activity is expected in the central region for UPC events. This can also be concluded from the emersion of the peak in the energy spectrum solely for hadron-like events in TS for $n_{sel} = 0$ and by comparing in figure 16 data to simulation.

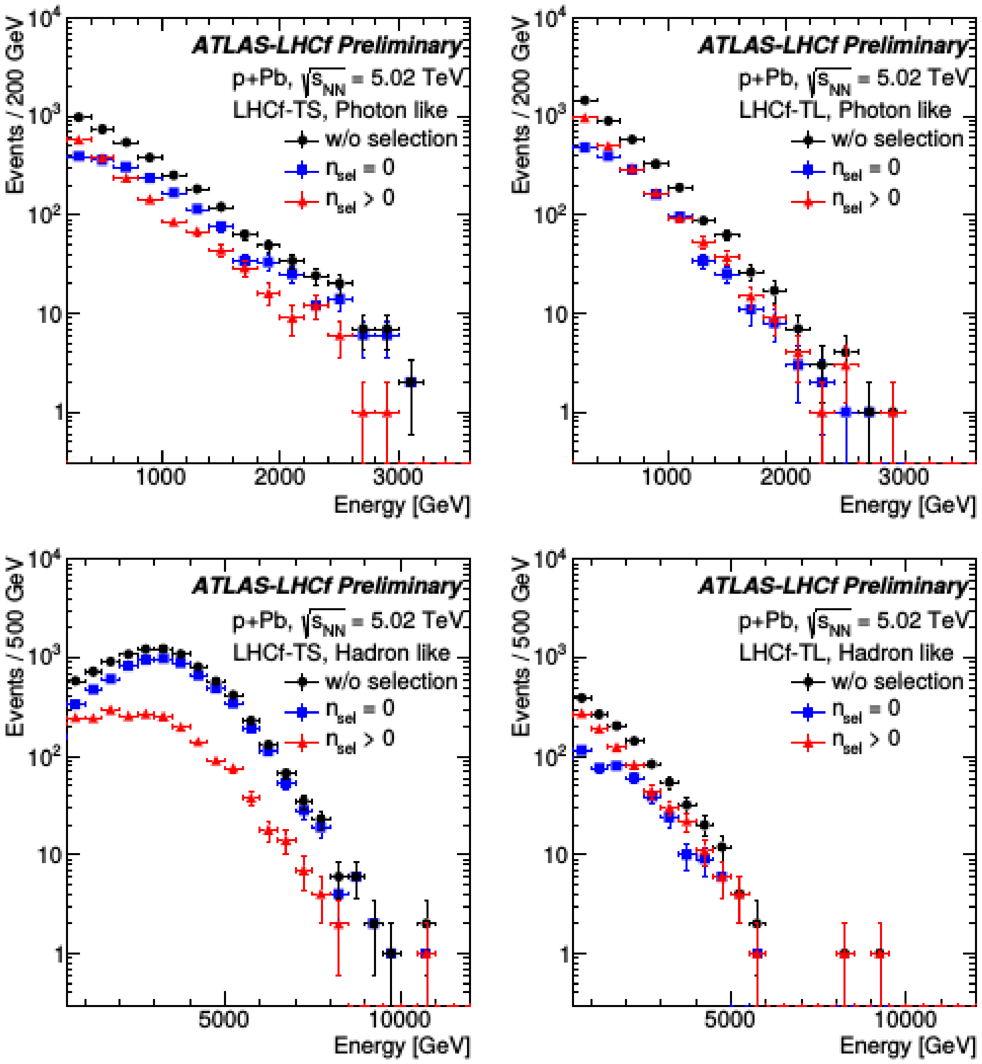

Figure 15: The energy spectra of the photon-like (top) and hardon-like (bottom) events measured by LHCf in TS (left) and TL (right) are shown as black circles. The effects of the finite energy resolution and non-uniformity of acceptance in pseudorapidity are not corrected for in these results. A classification based on the number of charged particle tracks in the central region reconstructed by ATLAS is done. [13]

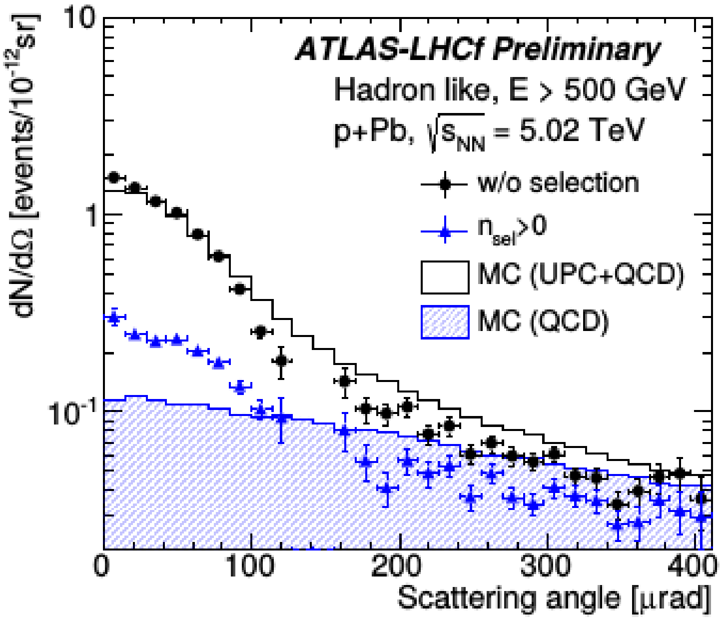

Figure 16: Scattering angle of the hadron-like events. The effects of the finite energy resolution and non-uniformity of acceptance in pseudorapidity are not corrected for in these results. All events from the common ATLAS and LHCf dataset are shown as black circles and the subset of those with charged particle tracks reconstructed in ATLAS are indicated by blue triangles. The data is compared to the Monte Carlo simulation of the processes corresponding to UPC and QCD (black) and QCD only (blue). The sum of UPC and QCD simulations is normalized to all data in the range from 0 rad to 120 rad. The detector response was not included in the simulation of the events. [13]

9 Exploratory analysis of events at ATLAS

In what follows we are going to describe the analysis done on the ATLAS side with the sole information form LHCf being trigger information. The strategy pursued was to compare distributions of kinematic variables of minimum bias events and LHCf-triggered events. The exploration of the data recorded by ATLAS had as a goal to identify kinematic variables sensitive to the trigger choice on the one hand and to make first physics statements on the other hand - this with the 2015 LHC p+p run in mind.

Antecedent to analysing any kinematic variables one should know the number of events that passed each trigger. This information is listed in table 1. We see that we have about 3.2 million events available in our dataset, of which about 2.5% and 4.1% triggered the EF-level MBTS and LHCf-trigger, respectively. Comparing the percentage of events that passed the EF-level MBTS-trigger to its L1 trigger, one perceives an important diminishment of events. This is insofar problematic, as in section 9.2 we are going to employ combined LHFf- and MBTS-triggers. We see that in table 1 merely one event simultaneously passed the *EF_L1MBTS_1_1_NoAlg* and the *EF_L1LHCF_NoAlg* trigger. Nonetheless, the 1.84% of events that passed the L1MBTS_1_1 and the *EF_L1LHCF_NoAlg* trigger at the same time enable us to make statistically relevant statements.

Trigger	Number of Events	Percentage
no trigger (all events)	$\approx 3.2 \times 10^6$	100%
EF_L1MBTS_1_1_NoAlg	$\approx 7.2 \times 10^4$	2.5%
EF_L1LHCF_NoAlg	$\approx 1.3 \times 10^5$	4.1%
L1MBTS_1_1	$\approx 2.3 \times 10^6$	71.9%
EF_L1MBTS_1_1_NoAlg && EF_L1LHCF_NoAlg	1	0%
L1MBTS_1_1 && EF_L1LHCF_NoAlg	$\approx 5.9 \times 10^4$	1.8%
EF_L1MBTS_1_1_NoAlg && L1LHCF	62	0%

Table 1: Number of events that pass the respective trigger. The rightmost column shows the percentage of events that passed a certain trigger. All events that were included in the *Good Run List* are considered.

9.1 Initial Exploration of various kinematic variables

Some variables exhibit stronger trigger dependencies than others. Finding the most sensitive one is, at this stage of research, a question of testing out which variable variates most under different trigger choices. We investigated many different kinematic variables and, for most of them, the choice of the trigger (MBTS or LHCf) produced no, insignificant, or hard to interpret variations of the variable's distribution.

We are going to exemplify the case of an insensible kinematic variable on the pseudorapidity η. In figure 17 is displayed the pseudorapidity distribution of tracks passing the cuts in section 7.1. We observe a slightly increased probability for tracks occurring in the negative η region (the proton going side) for the LHCf-trigger, when compared to the MBTS-trigger. This can, however, simply be explained by recalling that only the detector Arm2 was up and running during the common data taking and that Arm2 is placed on the $-\eta$ side of IP1. One can expect events firing off the Arm2 trigger also to produce a higher number of tracks in the $-\eta$ region in general; including the more central negative pseudorapidity region.

Finding no interesting patterns by solely investigating the pseudorapidity, we checked for interesting patterns in the scatter plot of transversal momentum p_T vs. η, figure 18. We were again not able to identify interesting differences between the LHCf-triggered and the MBTS-triggered events. We also analysed the transverse momentum of the tracks separately and looked at other variables such as, jet multiplicity and rapidity gaps. We found the most imminent differences between both triggers emerging in the track multiplicity distributions.

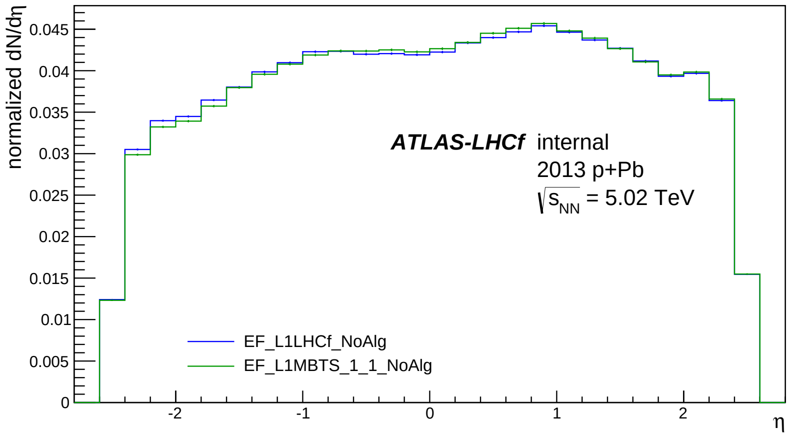

Figure 17: Pseudorapidity η distribution of reconstructed tracks that passed the track selection cuts described in section 7.1 for the given triggers. Both histograms have been normalized to unit area. Positive η corresponds to tracks on the lead remnant side. The pseudorapidity coverage amounted to $|\eta| < 2.5$.

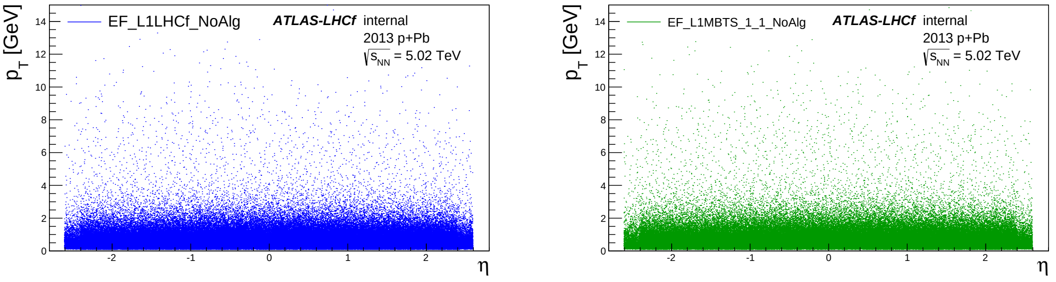

Figure 18: Scatter plots of transverse momentum p_T vs. pseudorapidity η for the LHCf-trigger (left) and the MBTS-trigger (right). The pseudorapidity coverage amounted to $|\eta| < 2.5$.

The track multiplicities for the EF-level triggers are shown in figure 19. We can recognize a clear difference in the slope of both distributions in the $10 < n_{sel} < 100$ regime. Moreover, a dip for $1 < n_{sel} < 10$ is present in the distribution for the MBTS-trigger, which we do not observe for the LHCf-trigger. We see also that both distributions have a similar slope for $n_{sel} \gtrsim 140$. An advantage of the track multiplicity being considered is its conceptual simplicity, when compared for example to the jet multiplicity or the rapidity gap. This feature facilitates immensely the interpretation of the produced histograms. In the next section we are going to focus on the track multiplicity for different triggers (EF and L1) and make first physics statements.

In the histograms in figure 19 and in all subsequent figures showing track multiplicities, the binning is two tracks per bin, with the exception of zero multiplicity events which have been put in a separate bin. This is motivated by the large share of events these zero multiplicity events constitute. To clarify, for each histogram the first non-empty bin is filled solely with events with $n_{sel} = 0$. The second bin is filled with $n_{sel} = 1$, 2 events, the third bin with $n_{sel} = 3$, 4 events and so on.

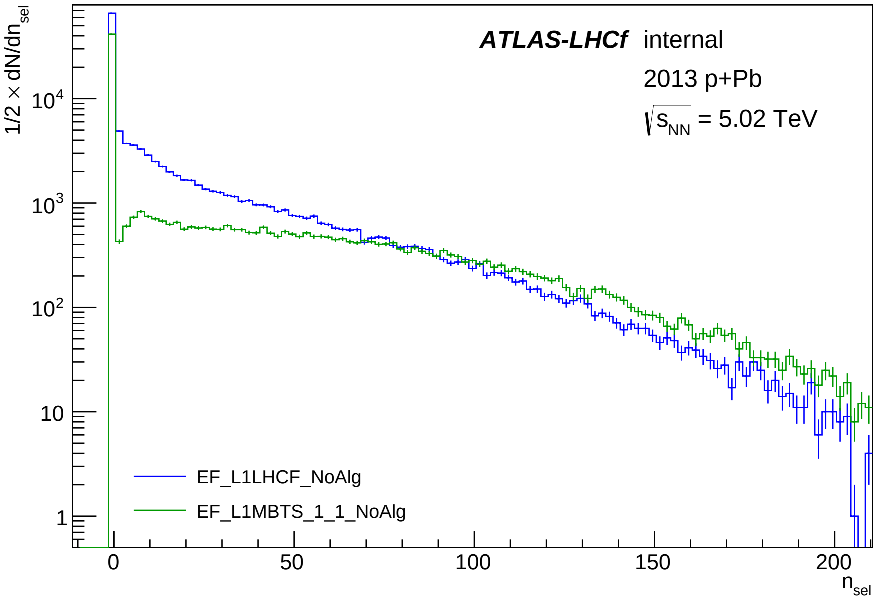

Figure 19: Track multiplicity distributions of tracks that were reconstructed in the Inner Detector of ATLAS.

9.2 Further investigation of the track multiplicity

We have seen in section 4 that a signature for UPC events is that they produce no tracks in the central region. This is corroborated by the conclusions we drew in section 8, especially from figure 16. Requiring $n_{sel} > 1$ eliminates the vast majority of UPC events. This means, that we only have to determine whether or not an event is diffractive or non-diffractive. For MBTS-triggered events we have the rapidity gap method described in section 7.2 that allows us to do this. The rapidity gap distributions for the MBTS and LHCf Event Filter level triggers are shown in figure 20. Especially for large rapidity gaps we observe a significant difference for the LHCf trigger between $\Delta\eta_{\mathrm{Pb}}$ and $\Delta\eta_p$. This feature is not present for the MBTS trigger. We should also note that for each trigger the last bin of the two rapidity gap distributions is equal. This is because a rapidity gap of $\Delta\eta_{\mathrm{Pb}} > 9.8$ means that no activity was recorded at ATLAS and entails that also $\Delta\eta_p > 9.8$ is the case.

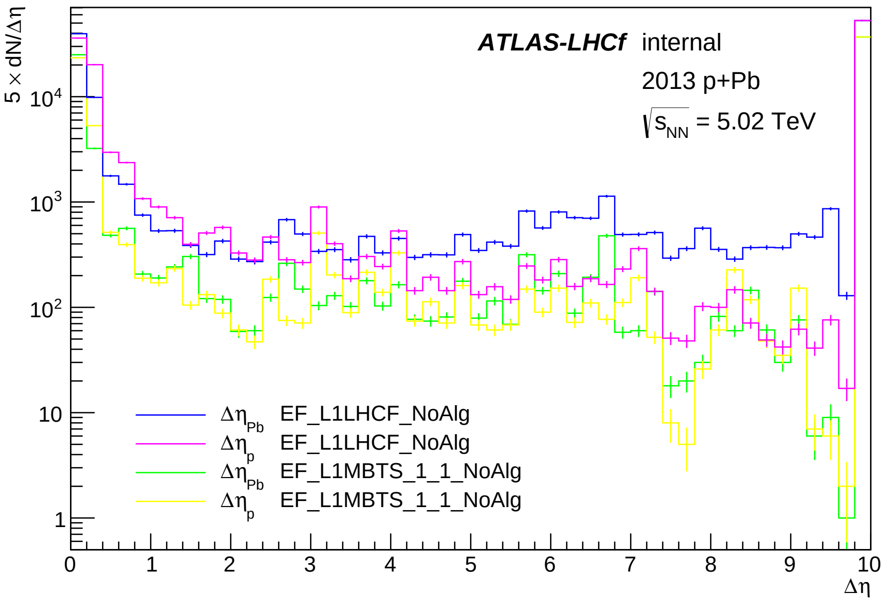

Figure 20: Distributions of reconstructed rapidity gaps on the ATLAS side.

In figure 21 we compare the track multiplicity distribution of minimum bias events to the one for minimum bias events on which the rapidity gap cuts described in section 7.3 have been applied. We see that for high track multiplicities the ratio of the two histograms tends to one. Implicating that high multiplicity events have no diffractive admixture. All events at $n_{sel} = 0$ pass the diffractive selection as no tracks means by definition the presence of a large rapidity gap. We expect tracks to lie outside of the tracker acceptance in such diffractive events. Furthermore, we observe an enhancement of the dip in the distribution for $n_{sel} < 10$. This feature is immanent to minimum bias events, which consist predominantly of non-diffractive events and which is further pronounced by applying the rapidity gap cuts.

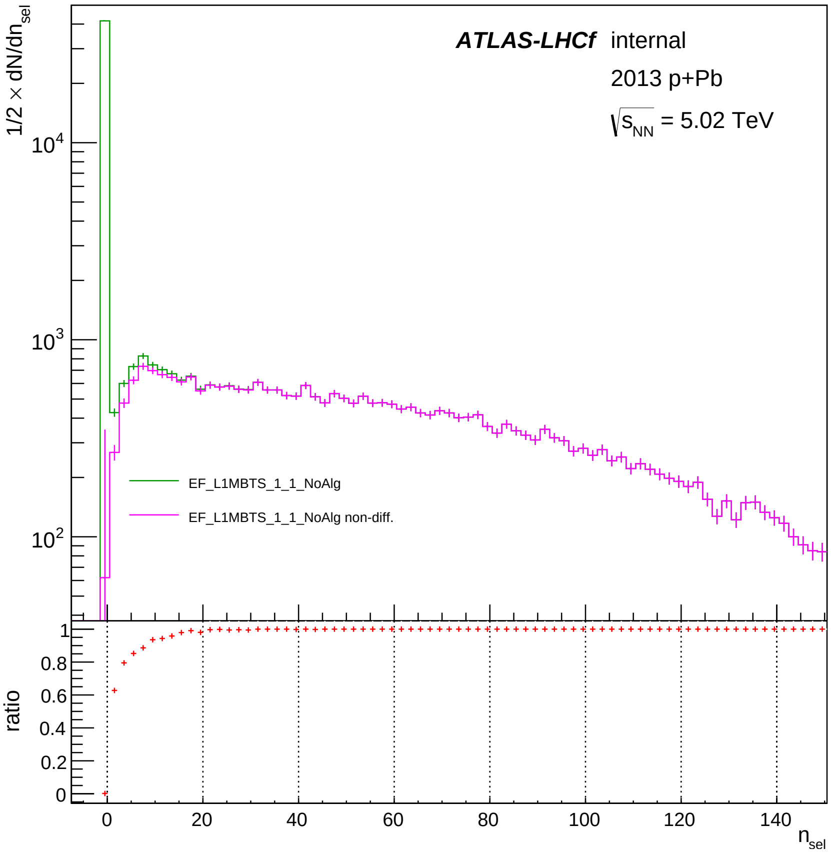

Figure 21: Comparison between the track multiplicity for EF-level MBTS trigger and the track multiplicity of non-diffractive events for the same trigger.

We did also apply the rapidity gap cuts to events triggered by *EF_L1LHCF_NoAlg*. The resulting effect on the distribution can be observed in figure 22 where we compare LHCf-triggered events to LHCf-triggered events that did pass the rapidity gap selection.

Similar to minimum bias events, we notice the appearance of a dip at $n_{sel} < 10$ for the events passing the diffractive rapidity gap selection and moreover that the $\Delta\eta$ cuts have no effect on high multiplicity events. These two qualities of the track multiplicity for the LHCf-triggered events, together with the fact that rapidity gaps are exponentially suppressed in non-diffractive events, let us conclude that rapidity gap cuts present an efficient method to distinguish between non-diffractive and diffractive events not only for MBTS events but also for LHCf-triggered events.

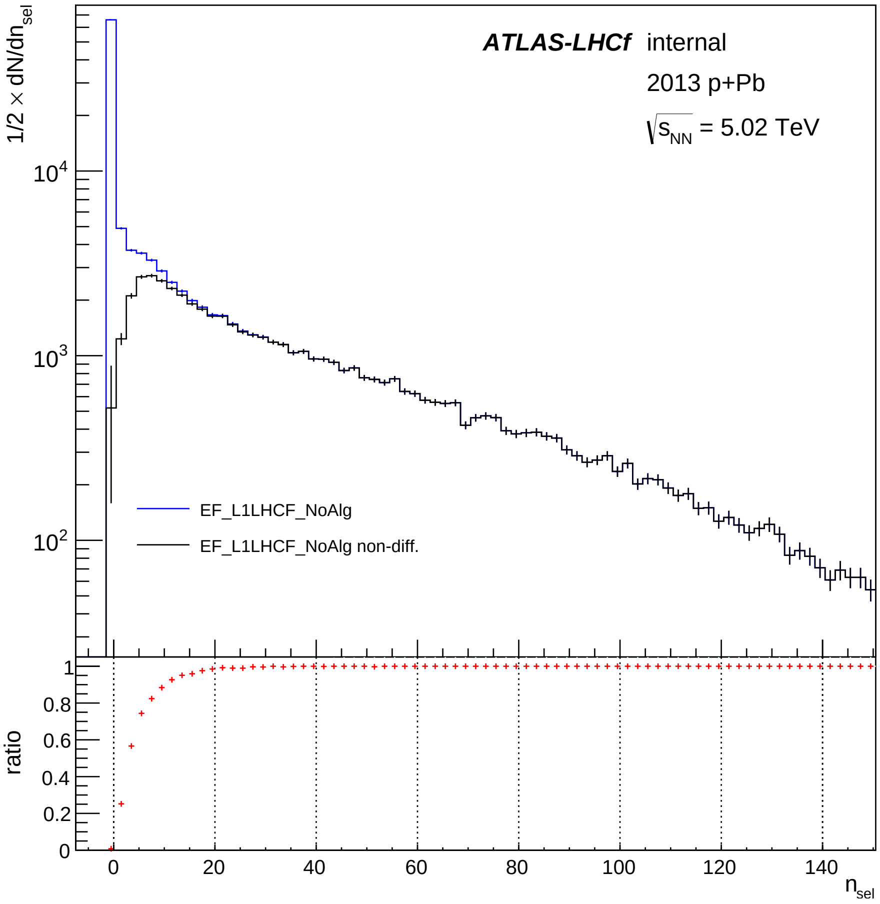

Figure 22: Comparison between the track multiplicity for EF-level LHCf trigger and the track multiplicity of non-diffractive events for the same trigger.

This last statement is further corroborated by considering the distributions in figure 23. Apart from the zero multiplicity events, the effect of imposing the *L1MBTS_1_1_NoAlg* trigger on LHCf-triggered events is very similar to applying rapidity gap cuts. This tells us that, when bearing in mind that MBTS identifies mostly non-diffractive QCD events, the rapidity gap method functions formidably on LHCf-triggered events in order to isolate diffractive events.

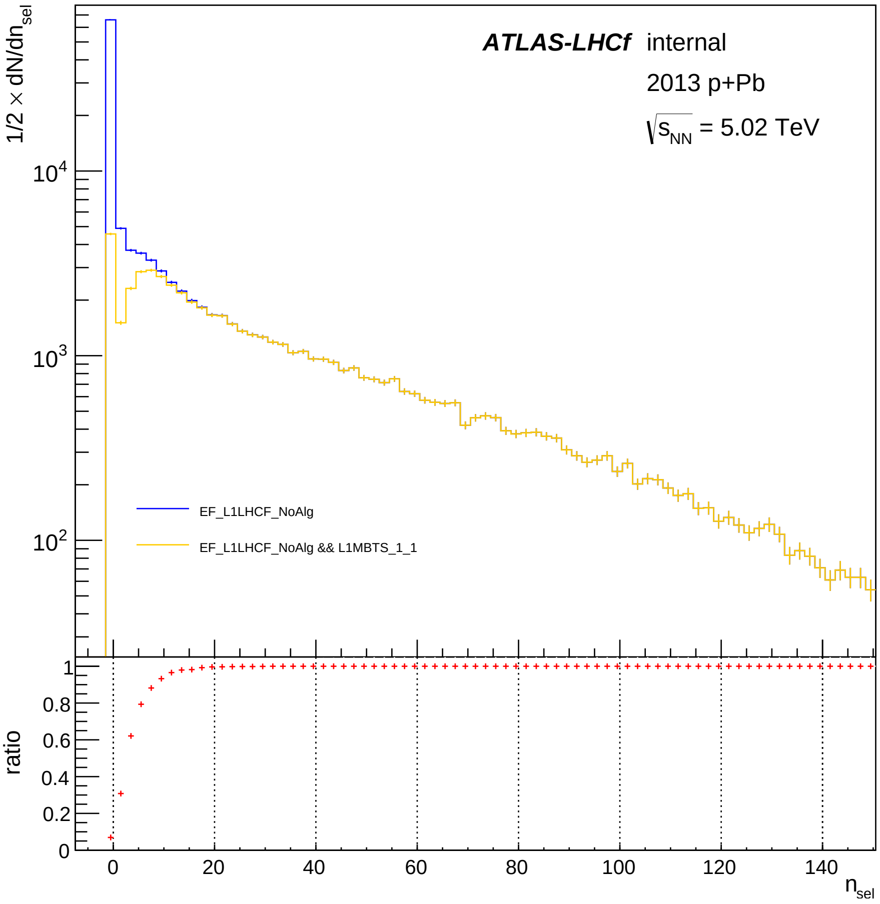

Figure 23: Comparison of the EF-level LHCf-trigger and the same trigger combined with the L1 MBTS-trigger.

We are now able to conclude that the absence of the dip in figure 19 is due to a higher efficiency of the *EF_L1LHCF_NoAlg* trigger to record diffractive events when compared to *EF_L1MBTS_1_1_NoAlg*-triggered events.

We note furthermore that for LHCf-triggered events with $n_{sel} > 30$, all events do also trigger *L1MBTS_1_1_NoAlg* (cf. ratio in figure 23) and by remembering in addition that these events are practically all of a non-diffractive nature (figure 22), we can conclude that the differences in shape of the distributions in figure 19 for $30 < n_{sel}$ stem from the lack of efficiency of *EF_L1MBTS_1_1_NoAlg* to select non-diffractive high multiplicity events.

10 Conclusions and Outlook

We have shown in this thesis, which constitutes a proof of feasibility of a future more comprehensive common ATLAS-LHCf data analysis on the 2015 p+p dataset, that through a correct trigger sharing procedure the successful matching of events recorded separately by ATLAS and LHCf enables both experiments to exchange reconstructed physical quantities. This is of utmost importance to LHCf, as information of the track multiplicity and rapidity gap presence in the central region of ATLAS permits a reliable distinction between non-diffractive, diffractive and UPC events.

We have specifically demonstrated that we were capable of distinguishing the diffractive and UPC processes from the non-diffractive ones in LHCf-triggered events by means of rapidity gaps. The importance of this becomes clear when inspecting the cross sections listed in table 2. The UPC processes, that belong to background in the analyses aiming to constrain cosmic-ray air shower models, dominate in the dataset taken in the p+Pb collisions. They represent, on the contrary, a negligible component of the p+p dataset. Since diffractive and non-diffractive processes are treated differently in interaction models, such a data driven event separation in a common p+p dataset, as presented in this thesis, will constitute a major benefit to further improving hadronic interaction models used in cosmic ray air shower simulations.

	inelastic	diffractive	UPC
proton-lead	2b	≈40mb	180mb
proton-proton	80mb	≈22mb	0.02mb

Table 2: The first column shows the simulated production cross section for p+Pb and p+p collisions at $\sqrt{s_{p\mathrm{Pb}}} = 5.02$ TeV and $\sqrt{s_{pp}} = 13$ TeV. Columns 2 and 3 state the share of diffractive and UPC events for the two different collisions.

With the need of effectively separating non-diffractive and diffractive events in the 2015 pp dataset, improving the identification of rapidity gaps in the central region is most decisive. A first step to such an amendment would be to look not only for rapidity gaps on the edges of the ATLAS detector (as described in section 7.2) but to scan the whole $|\eta| < 4.9$ range for rapidity gaps.

References

[1] Measurement of long-range pseudorapidity correlations and azimuthal harmonics in $\sqrt{s_{\mathrm{NN}}}$=5.02 TeV proton-lead collisions with the ATLAS detector. Technical Report ATLAS-CONF-2014-021, CERN, Geneva, May 2014.

[2] The way to collisions, step by step. En route vers les collisions, étape par étape. (BUL-NA-2009-349. 43/2009. 44/2009. 43/2009):1, Oct 2009. Cover article.

[3] G. Aad, B. Abbott, J. Abdallah, A. A. Abdelalim, A. Abdesselam, O. Abdinov, B. Abi, M. Abolins, O. S. AbouZeid, H. Abramowicz, and et al. Rapidity gap cross sections measured with the ATLAS detector in pp collisions at sqrt{s} = 7 { TeV}. *European Physical Journal C*, 72:1926, March 2012.

[4] G. Aad, B. Abbott, J. Abdallah, A. A. Abdelalim, A. Abdesselam, O. Abdinov, B. Abi, M. Abolins, H. Abramowicz, H. Abreu, and et al. Performance of the ATLAS Trigger System in 2010. *European Physical Journal C*, 72:1849, January 2012.

[5] G.L. et al. Aad. Performance of the ATLAS Trigger System in 2010. *The European Physical Journal C*, 72(1), 2012.

[6] D. et al. Acosta. Central pseudorapidity gaps in events with a leading antiproton at the fermilab tevatron $\overline{p}p$ collider. *Phys. Rev. Lett.*, 91:011802, Jul 2003.

[7] E.-J. Ahn, R. Engel, T.-K. Gaisser, P. Lipari, and T. Stanev. Cosmic ray interaction event generator SIBYLL 2.1. *Phys.Rev.D*, 80(9):094003, November 2009.

[8] J. Allen, A. Castellina, R. Engel, K. Kasahara, S. Knurenko, T. Pierog, A. Sabourov, B. T. Stokes, R. Ulrich, T. Sako, and S. Ostapchenko. Air shower simulation and hadronic interactions. In *European Physical Journal Web of Conferences*, volume 53 of *European Physical Journal Web of Conferences*, page 1007, June 2013.

[9] S Ask, D Berge, P Borrego-Amaral, D Caracinha, N Ellis, P Farthouat, P Gãllnö, S Haas, J Haller, P Klofver, A Krasznahorkay, A Messina, C Ohm, T Pauly, M Perantoni, H Pessoa Lima Junior, G Schuler, D Sherman, R Spiwoks, T Wengler, J M de Seixas, and R Torga Teixeira. The atlas central level-1 trigger logic and ttc system. *Journal of Instrumentation*, 3(08):P08002, 2008.

[10] Vincenzo Barone and Enrico Predazzi. *High-Energy Particle Diffraction.* Springer Science, 2002.

[11] John T. Behrens. Principles and procedures of exploratory data analysis. *Psychological Methods*, 2(2):131–160, 1997.

[12] C. A. Bertulani, S. R. Klein, and J. Nystrand. Physics of Ultra-Peripheral Nuclear Collisions. *Annual Review of Nuclear and Particle Science*, 55:271–310, December 2005.

[13] Lorenzo Bonechi, David Berge, Menjo Hiroaki, David Salek, Sako Takashi, and Pedro Miguel Zuidberg Dos Martires. The First Analysis of the Combined ATLAS-LHCf Data Recorded During the p+Pb Collisions at $\sqrt{s_{NN}} = 5.02$ TeV. Technical Report ATL-COM-PHYS-2015-424, CERN, Geneva, May 2015.

[14] F. W. Bopp, J. Ranft, R. Engel, and S. Roesler. Antiparticle to particle production ratios in hadron-hadron and d-au collisions in the dpmjet-iii monte carlo model. *Phys. Rev. C*, 77:014904, Jan 2008.

[15] Geoffrey F. Chew and S. C. Frautschi. Principle of equivalence for all strongly interacting particles within the s-matrix framework. *Phys. Rev. Lett.*, 7:394–397, Nov 1961.

[16] The ATLAS Collaboration. The ATLAS Experiment at the CERN Large Hadron Collider. *Journal of Instrumentation*, 3(08):S08003, 2008.

[17] The ATLAS Collaboration. Charged-particle multiplicities in pp interactions measured with the ATLAS detector at the LHC . *New J. Phys.*, 13(5):053033, may 2011.

[18] The ATLAS collaboration. Performance of the ATLAS Minimum Bias and Forward Detector Triggers in pPb collisions. 2013.

[19] The LHCf Collaboration. The LHCf detector at the CERN Large Hadron Collider. *Journal of Instrumentation*, 3(08):S08006, 2008.

[20] The LHCf Collaboration. Measurement of forward neutral pion transverse momentum spectra for $\sqrt{s} = 7$ TeV proton-proton collisions at the LHC. *Phys. Rev. D*, 86:092001, Nov 2012.

[21] P.S. Datte, J.-F. Beche, M. Haguenauer, P.F. Manfredi, M. Manghisoni, J.E. Millaud, M. Placidi, L. Ratti, V.J. Riot, H. Schmickler, V. Speziali, G. Traversi, and W.C. Turner. Initial test results of an ionization chamber shower detector for a LHC luminosity monitor. *IEEE Trans. Nucl. Sci.*, 50(2):258–262, apr 2003.

[22] H.-J. Drescher and G. R. Farrar. Dominant contributions to lateral distribution functions in ultra-high energy cosmic ray air showers. *Astroparticle Physics*, 19:235–244, May 2003.

[23] David d'Enterria, Ralph Engel, Tanguy Pierog, Sergey Ostapchenko, and Klaus Werner. Constraints from the first {LHC} data on hadronic event generators for ultra-high energy cosmic-ray physics. *Astroparticle Physics*, 35(2):98 – 113, 2011.

[24] R. Engel, T. K. Gaisser, P. Lipari, and T. Stanev. Proton-proton cross section at s˜30 TeV. *Phys. Rev. D*, 58(1):014019, July 1998.

[25] Ralph Engel, Dieter Heck, and Tanguy Pierog. Extensive Air Showers and Hadronic Interactions at High Energy. *Annual Review of Nuclear and Particle Science*, 61(1):467–489, 2011.

[26] Adriani et al. LHCf detector performance during the 2009-2010 LHC run. *Int. J. Mod. Phys. A*, 28(CERN-PH-EP-2013-142. 25):1330036. 26 p, Jul 2013.

[27] K Kawade et al. The performance of the LHCf detector for hadronic showers. *Journal of Instrumentation*, 9(03):P03016, 2014.

[28] Lyndon Evans. The large hadron collider. *New Journal of Physics*, 9(9):335, 2007.

[29] Andrew Gelman. Exploratory Data Analysis for Complex Models. *Journal of Computational and Graphical Statistics*, 13(4):755–779, 2004.

[30] K. Goulianos. Diffraction in QCD. *ArXiv High Energy Physics - Phenomenology e-prints*, March 2002.

[31] K Goulianos. Renormalized Diffractive Parton Densities. *PoS*, DIFF2006:044, 2006.

[32] Kenneth Greisen. End to the cosmic-ray spectrum? *Phys. Rev. Lett.*, 16:748–750, Apr 1966.

[33] M. J. Herrero. The Standard Model. *ArXiv High Energy Physics - Phenomenology e-prints*, December 1998.

[34] Victor Franz Hess. Über Beobachtungen der durchdringenden Strahlung bei sieben Freiballonfahrten. *Physikalische Zeitschrift*, 13, 1912.

[35] F. Hügging and Atlas Collaboration. The ATLAS Pixel Insertable B-layer (IBL). *Nuclear Instruments and Methods in Physics Research A*, 650:45–49, September 2011.

[36] Peter Jenni, Marzio Nessi, and Markus Nordberg. Zero Degree Calorimeters for ATLAS. Technical Report LHCC-I-016. CERN-LHCC-2007-001, CERN, Geneva, Jan 2007.

[37] K. Taki et al. Trigger and background study for the LHCf experiment. *Presented at the "31st International Cosmic Ray Conference", Lodz (Poland)*, 2009.

[38] K.-H. Kampert. Cosmic Rays from the Knee to the Ankle Status and Prospects. *Nuclear Physics B Proceedings Supplements*, 165:294–306, March 2007.

[39] K.-H. Kampert and A. A. Watson. Extensive air showers and ultra high-energy cosmic rays: a historical review. *European Physical Journal H*, 37:359–412, August 2012.

[40] R. Kwee and ATLAS Collaboration. Minimum Bias Triggers at ATLAS. In *Physics at LHC 2008*, page 117, 2008.

[41] Louis Lyons. Bayes and Frequentism: a particle physicist's perspective. *Contemporary Physics*, 54(1):1–16, 2013.

[42] Zachary Marshall and the Atlas Collaboration. Simulation of pile-up in the atlas experiment. *Journal of Physics: Conference Series*, 513(2):022024, 2014.

[43] J. Matthews. A heitler model of extensive air showers. *Astroparticle Physics*, 22(5–6):387 – 397, 2005.

[44] A. Mücke, R. Engel, J. P. Rachen, R. J. Protheroe, and T. Stanev. Monte Carlo simulations of photohadronic processes in astrophysics. *Computer Physics Communications*, 124:290–314, February 2000.

[45] M Nagano. Search for the end of the energy spectrum of primary cosmic rays. *New Journal of Physics*, 11(6):065012, 2009.

[46] S. Ostapchenko. QGSJET-II: towards reliable description of very high energy hadronic interactions. *Nuclear Physics B Proceedings Supplements*, 151:143–146, January 2006.

[47] J R Pater. The atlas semiconductor tracker operation and performance. *Journal of Instrumentation*, 7(04):C04001, 2012.

[48] D. Perepelitsa, B. Cole, and P. Steinberg. Centrality Determination in the 2012 and 2013 p+Pb data in ATLAS. Technical Report ATL-COM-PHYS-2013-588, CERN, Geneva, May 2013.

[49] Adam Perer and Ben Shneiderman. Integrating Statistics and Visualization: Case Studies of Gaining Clarity During Exploratory Data Analysis. In *Proceedings of the SIGCHI Conference on Human Factors in Computing Systems*, CHI '08, pages 265–274, New York, NY, USA, 2008. ACM.

[50] Tanguy Pierog. LHC results and High Energy Cosmic Ray Interaction Models. *J. Phys.: Conf. Ser.*, 409:012008, feb 2013.

[51] S. Roesler, R. Engel, and J. Ranft. *The Monte Carlo Event Generator DPMJET-III*, page 1033. 2001.

[52] The Pierre Auger Collaboration. The Pierre Auger Cosmic Ray Observatory. *ArXiv e-prints*, February 2015.

[53] John W. Tukey. *Exploratory Data Analysis.* Pearson, 1977.

[54] John W. Tukey. We Need Both Exploratory and Confirmatory. *The American Statistician*, 34(1):23–25, 1980.

[55] R. Ulrich, R. Engel, S. Müller, F. Schüssler, and M. Unger. Proton-Air Cross Section and Extensive Air Showers. *Nuclear Physics B Proceedings Supplements*, 196:335–340, December 2009.

[56] R. Ulrich, R. Engel, and M. Unger. Hadronic multiparticle production at ultrahigh energies and extensive air showers. *Phys. Rev. D*, 83(5):054026, March 2011.

[57] C. F. von Weizsacker. Radiation emitted in collisions of very fast electrons. *Z. Phys.*, 88:612–625, 1934.